ELECTROMAGNETICALLY ACTUATED DEVICES FOR OPTICAL COHERENCE TOMOGRAPHY APPLICATIONS

by

Hans P. Hu

Presented to the Faculty of the Graduate School of

The University of Texas at Arlington in Partial Fulfillment

of the Requirements

for the Degree of

DOCTOR OF PHILOSOPHY

THE UNIVERSITY OF TEXAS AT ARLINGTON

May 2007

DEDICATION

To the memory of my grandfather, Mr. Hu, Yu-nien, for his relentless love, support and encouragement.

ACKNOWLEDGEMENTS

First of all, I would like to thank my advisor Dr. J.-C. Chiao for giving me flexibility on exploring my own ideas and experiments under his guidance and support. I also want to thank Dr. Digant Dave for letting me do experiments in his lab for the past one and half years. Also I like to thank Dr. Bredow, Dr. Stelmakh, and Dr Butler for being a member of my dissertation committee.

Also I appreciate members in Dr. Dave's lab: Asif Rizwon, Nidhi Medah for their valuable inputs and help on the OCT part of the experiments.

I would like to thank mechanist Mr. Tom Leid for fabricating many tools and parts during the course of my experimentation.

Finally, I want to share my achievement with my parents and sister Betty for their support and encouragement.

January 3, 2007

ABSTRACT

ELECTROMAGNETICALLY ACTUATED DEVICES FOR OPTICAL COHERENCE TOMOGRAPHY APPLICATIONS

Publication No. _____

Hans P. Hu, PhD.

The University of Texas at Arlington, 2007

Supervising Professor: Dr. J.-C. Chiao

A fast optical scanning device has always been desired for numerous applications such as biomedical imaging, optical communications, and variety of sensing and actuating applications. This dissertation presents a new scanning device operated using external magnetic field with low cost, high function versatility, low field strength, and low power consumption. The design architecture of this device shows its potential for in vivo application with an advantage that addresses the concern of safety. Materials properties are examined using alternating gradient magnetometer(AGM) to verify its performance. Pressure and temperature invariant fabrication processes are implemented to make this device without complicated equipments. The development and

construction is discussed from materials and device performance properties. In this dissertation, the device is also explored from the endoscopic point of view for in vivo imaging: device functionalities and its constraints as an endoscopic scanner. Preliminary static and dynamic performance data are shown to demonstrate its ability as an optical scanner with compromising speed and scanning range. To test for its applicability in imaging application, the device is made compatible with an optical imaging system, namely, optical coherence tomography (OCT). OCT is a relatively new imaging modality capable of cross sectional imaging with resolution in micrometers. The setup used to test the optical scanner is an OCT system which retrieves information about the depth resolved reflectivity profile using the spectral domain information of the reflective light. This report is started with a review of magnetics, which explains the fundamental governing principles behind the optical scanner. In the second section technical information about the optical scanner is entailed. Finally, the investigation on the suitability of the scanner for OCT application is performed.

TABLE OF CONTENTS

LIST OF ILLUSTRATIONS

Figure Page

LIST OF TABLES

CHAPTER 1

INTRODUCTION

1.1 Overview

Miniaturized devices have been applied to many different fields for the advantages such as small feature sizes and low power consumption. In this chapter, some basics about endoscope are presented. Due to the limitations of the traditional endoscopes miniaturized devices are proven to be effective in solving the difficulties and limitations on operating the traditional endosopes. Finally a comparison on different miniaturized devices based on several actuation technologies is done.

1.1.1 Endoscope Basics

Endosope is a tool for physicians and medical doctors to take images or do surgery on traumas and diseases on the surface of organs inside the bodies of living organs. Endoscopes allow the delivery of the electromagnetic waves inside the bodies; hence doctors can use the view field of endoscope to do the medical manipulations.[1] Traditional endoscopes are rigid endoscopes composed of compounded optical lenses, and the scope allows the insertion of the device itself inside bodies and the rotation of the scanning head by manipulating the external mechanical tool. Optical fiber based endoscopes or flexible endoscopes are the improved endoscopes, which utilizes the

optical fibers to deliver the light source and performs the scanning by moving the head of the endoscope, and the main advantage of a flexible endoscope is its ability to be bended, therefore, greatly reduce the chance of getting injuried.[2] Also the motivation of high resolution endoscopy has led to the rapid advances in the performance of fiber imaging guides, which uses an optical fiber to transmit images.[3] Both rigid and flexible endoscopes have two main limitations, namely, the view field of the scanning area by physicians and manipulation space inside bodies. Since traditional rigid and flexible endoscopes are bulky they are difficult to perform a precise minimally invasive surgery because the movement of the rigid endoscope to scan over a broader surface is limited, and also the scanning capability is greatly reduced by the volume available to perform scanning or other operations.[4]

1.1.2 Motivation for Device Miniaturization

MEMS devices and fiber optical devices turn out to be good solutions to resolve the limitations of limited space in performing minimally invasive scanning. MEMS technologies allow the device miniaturization, cost reduction, and high precision, and those features can help medical doctors and physicians to relieve the limitation on performing image scanning and surgeries.[5] There are efforts to improve the traditional endoscopes by means of MEMS technologies, namely, the micro motor based endoscope, which uses a 2mm micro-motor to rotate the scanning head automatically, "hyper endoscope" which uses minimum of wiring to drive multi-micro actuators, and a robotic endoscope system capable of wide-angle view using wedge prisms.[4, 6, 7]

Implementation of endoscope using miniaturizing technologies require some components such as micro-mirror actuation and light guiding optics. The MEMS

actuation technologies have been developed for some years and have been applied in many fields such as military applications, optical scanning, automation, data storage and etc….. The optical MEMS, in particular, has been a hot research topic recently for its potential in an all optical imaging system because it provides high integration, higher bandwidth transmission, low cost and high versatility in terms of implementations and functions.[8]

1.1.3 Overview of OCT Systems

The advantages of miniaturizing devices can provide scanning solutions for OCT systems. In order to grasp a good sense of the requirement of the scanner for OCT imaging application, an overview of different type of OCT system is given in this subsection.

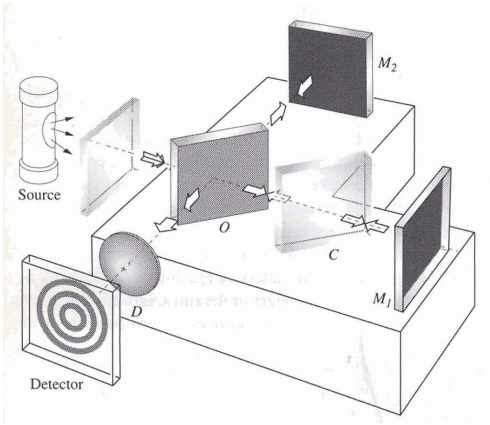

Figure 1.1 A layout diagram of Michaelson's interferometer[9].

Michaelson's interferometer is the backbone of OCT systems, and it is as shown in figure 1.1.[9] A Michaelson's interferometer is composed of a light source, a beam slitter, and two mirrors. With one mirror positions in the reference path and another one in the sample path, lights of reference path and sample path are reflected. Under the

condition that both reference and sample paths are matched up, interference pattern will then show in the detecting path when a piece of paper is blocked on its way. The original design of michaelson's interferometer, though an important system for later technologies, has its draw back: the beam splitter plate itself serves as a Fabry-Perot interferometer, which has effects on its bandwidth, signal magnitude of the interference signals. Also, the entire system is bulky, and it is not suitable for modern application needs. Michaelson's interferometer has been applied to microscopy, measurement of optical group refractive index, measurements of choroidal perfusion, remote distance sensing, and space sciences. The application of miachaelson's interferometer in biomedical imaging is a fifteen year old imaging modality. Compared to other imaging modalities such as ultrasound, magnetic resonance imaging (MRI), optical interfrometry provides finer spatial resolution; however, the drawback is that its depth of penetration is rather limited due tissue scattering and absorption. Dr Fujimoto has been a pioneer in the field of applying michaelson's interferometer for biomedical imaging applications. From Dr. Fujimoto's lab, the first biomedical interfrometry system is built for ophthalmology application and it is shown in figure 1.2.[10]

As compared to the original michaelson's interferometer, the medical interfrometry is a compact, all optical fiber based system with movable mirror in the reference arm for depth scan purpose. Difference regions of eye ball can be imaged due to the clear mismatches in optical index refraction of layers in an eye ball. The signal to noise ratio of 95 dB is achieved.

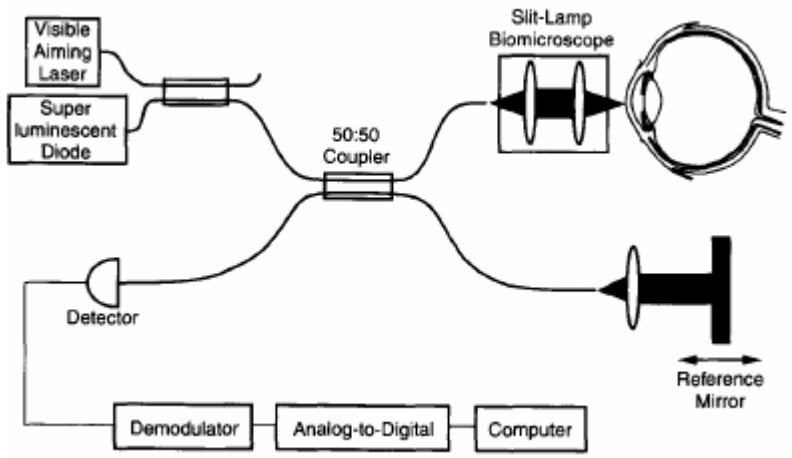

Figure 1.2 A setup of time-domain OCT built for ophthalmologic applications[10].

Since then various modes of functional medical interfrometry have been developed such as Doppler OCT and polarization based OCT systems.[11, 12] Doppler effect is a well known effect, which explains the phenomena of frequency shift of waves due its impingement on moving objects. By taking advantages of high resolution monitoring due to coherence gating, velocity in the range of less than 20 um to more than 10 cm/s can be measured. An example of application using Doppler OCT is to detect the blood flow. The physical principle of Doppler OCT is the same as a regular OCT system. The essence of Doppler OCT lies in the detection of the frequency shift in the interference fringes, which can be translated into velocity measurement by the following equation

$$v = \frac{f_s \lambda_0}{2 n_s \cos\theta} \tag{1.1.1}$$

where f_s is the frequency shift, λ_o is the center wavelength of light source, n_s is the local index refraction of sample, and ɵ is the angle between ample arm beam and the direction of the flow.

Polarization OCT is another widely implemented OCT imaging system by utilizing the polarization of light property. This imaging modality can visualize the detailed information of structure of some tissues which exhibit birefringence such as collagen fibrils, microtubules, actin, and myosin filaments. The implementation of a polarization system is slightly different than the ordinary OCT system.

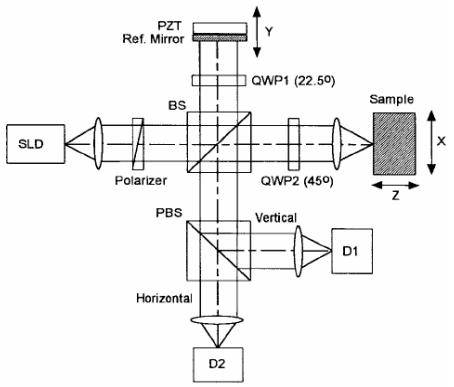

Figure 1.3 an example of experimental setup for polarization OCT system[12].

Figure 1.3 depicts an example of system setup for polarization OCT. The subtle difference of this imaging modality is the following: a zeroth-order quarter-wave plate (QWP1) transforms the horizontally polarized input light of reference path into 45° linearly polarized light. A quarter-wave plate (QWP2) transforms the horizontally polarized input light of sample path into circularly polarized light. The light back-reflected from sample is an unknown elliptically polarized light. Interference is observed when the difference in sample path and reference path is within the coherence length of

the broadband light source. At the detecting end a polarizing beam splitter PBS separates the detecting light into vertical and horizontal components, which can be detected by the respective detector.

Spectral-domain OCT (SD-OCT) is another type of OCT imaging system, which interrogates tissues by utilizing the spectral property of light. As compared with a time-domain OCT system, SD-OCT provides faster imaging speed, elimination of scanning device in the reference arm and more stable and consistent imaging quality. In the next sub-section, a conclusion is given to emphasis the content of this dissertation.

1.2 Summary and Conclusion

In this chapter, the scope of the content of this dissertation is illustrated. An endoscopic basics is given in order to illustrate the constraints of tools in the field of endoscopy. Miniaturizing devices such as MEMS devices and fiber optical devices have their advantages in the field of endoscopy because they provide small dimension profiles, fast speed, and high precision. One of the main objectives of this research is to build a miniaturized scanning device for optical coherence tomography (OCT) system; therefore an of view of different configuration of OCT systems were given for the better understanding of system requirements and limitations.

The flow of this dissertation is structured as the following. In chapter 2, a survey of optical scanners based of different actuation schemes is given. Magnetic actuation is considered to construct a fiber optical scanner and the advantages of the devices are addressed from the device and material points of view. Static and dynamic characterizations are performed to justify its capability,

and potential applications for the devices are explored. Chapter 3 is dedicated for the investigation of the electromagnetically actuated devices from OCT imaging application. A brief review of existing scanning probes is given first as an introduction to the magnetic scanning probe, which is interrogated using a spectral OCT system. Related issues regarding OCT imaging are also discussed. What if the fiber optical device is not suitable for OCT imaging? Ch 4 gives an alternative solution using magnetic actuation for OCT imaging. And finally, a conclusion is given to summarize the dissertation and some possible future works are pointed out.

CHAPTER 2

MINIATURIZED OPTICAL SCANNER

2.1 Overview

Compact optical devices, related fiber optic systems and MEMS(MicroElectroMechanicalSystems) have drawn much attention in fields requiring high integration and bandwidth transmission, low cost and high versatility in terms of implementation and functions[8]. Fiber optical devices and systems have found applications in actuators and sensors such as optical communications for signal switching and optical amplitude modulating[13], biomedical imaging application for taking images or doing surgery on traumas and diseases on the surfaces of organs inside the bodies of living beings[14, 15] biomolecular detection with rapidity, sensitivity, and selectivity in combination with mass spectrometry[16] and magnetic field sensing for transportation, navigating, current sensing, and magneto-metering applications[17-19]. In this section a survey of comparison of different optical scanning schemes is given and discussed. From the standpoint of view of device architecture and functions, this section explores the potential opportunities of the magnetic scanner for the targeting endoscopic application.

2.2 Survey of different types of optical scanners

Small dimensions and light weight of optical fiber have attracted a lot of researcher's attention to construct sensors and actuators. By mounting an optical fiber on top of an

actuator, a fiber optical sensor or actuator can readily be realized. Table 2.1 summarizes the performance characteristics of sensors and actuators built upon different technology schemes. The displacement capability is not specified because that's not a concern for their application.

Due to the nature of different technology schemes, which provide a variety of performance requirements suitable for different applications. For instance, piezoelectric material based device, although provided with small displacement, is capable of more precise linear displacement. Piezoelectric effect is a phenomena, in which when a voltage is applied to piezoelectric materials such as lead zirconate titanate (PZT) and polyvinylidene fluoride (PVDF), and also, when mechanical stress is applied to piezoelectric materials voltage signal can get induced. The physical principle behind piezoelectric actuation is due to non-uniform distribution of charge in material crystals: a voltage source causes re-distribution of electrons and reshape of crystal, that gives rise to the change in material dimensions; the inverse is true, the dimension of piezoelectric material changes when subjected to mechanical stress, and that give rise to the induction of voltage signal.

Electro-static actuators are based on columbic attractive and repulsive forces. The advantage of electro-static actuators is that zero power is consumed since no physical electric current is present; however, its input voltage is often higher than most of other actuation schemes. Asymmetric thermal arm and bilayer structure are two commonly seen thermal actuators. In asymmetric thermal arm actuator, when electric current flow a thin arm and a thick arm in sequence, encounters different level of resistivity.

Table 2.1 Comparison of different actuation schemes: speed, power, and device dimensions

Actuation schemes	Size/ Materials	Power /voltage	Speed/ Motion	References
Piezo-Electric	PZT (6.4mmX 38.1mm)	300V	100Hz 1mm	[14]Boppart
Electro-Static Comb Drive		80V	200-10KHz	[24] Lee
Electro-Thermal	L=5500μm ,w=20μm ,d=45 μm	5280mW (210mA)	20Hz 140μm	[25] Cochran
Electro-Static		75V	>100Hz	[26] Herding
Electro-Magnetic	NiFe W=9mm L=43mm	9mW	>500Hz	[27] Nagoka

The temperature in the thinner section of the arm is higher. Because of the difference in thermal coefficients of two arms, translational motion of the arm is induced. Similarly with bi-layer structure actuator, when electric current flow through a stack of two materials with different thermal coefficients the entire structure is bent due to the difference in degree of thermal expansion. Electro thermal actuation, an electric current driven scheme, can consume power in thousands of watts. which is highly unsuitable for medical endoscopic application because high voltage or high power consumption could trigger hazards.

Technologies schemes such as piezoelectric, electrostatic comb drive, electro-thermal actuation can readily be used with an application of voltage source; however, these actuation schemes generally requires voltage input in tens of volts, which could cause potential damages on surrounding environment without proper isolation swhen used in application such as scan for endoscopic imaging.

In contrary, electromagnetic actuation consumes relatively smaller power while provides moderate speed. Moreover, the force of electromagnetic actuation is in the range of tens of μN, which can be compensated for a desired combination of device dimensions and speed; however, its suitability and practicality for optical imaging are yet being determined. In the next section a detailed discussion on magnetic devices is given. First a brief magnetic theory is reviewed to grasp the fundamentals of magnetics, which is the origin of all magnetic devices. Secondly, a summary of contemporary magnetic optical scanners and their applications is reviewed, and their fabrication process is also discussed. Thirdly, the measurement of magnetic field strength is done using hall-effect magnetic probe. Fourth, a treatment of theory and physical principle is given to get accountability of mathematical support of experiments: static and dynamic analysis. Finally, the design of electromagnetic scanner using optical fiber as scanner and wave-guiding mechanism is presented.

2.3 Electromagnetically Actuated Devices

Magnetics is a branch of science which has long been utilized in developing many devices such as magnetic recorder, electric transformers, electric motors, and others. The phenomenon of interaction between an external magnetic field and a magnetic medium has played a critical role in the functionality of these devices. An molecular level of treatment is given in order to grasp the fundamental behavior of magnetic materials and its function in devices. Magnetic force, in particular, has been the focus in the developing of our scanning device with fast scanning speed and long range, which ultimately determines the selection of magnetic materials.

2.3.1 Review of Magnetic Theory

Compass is a well-known navigation tool composed of a natural magnetic lobestone, which tries to align itself with the direction of earth's magnetic field. The behavior of the magnetic lobestone can be delineated by how magnetic field of earth influence the magnetic materials. Figure 2.1 shows different cases of magnetization upon different medium. Under vacuum condition as shown in Figure 1(a) the magnetic flux is related to the magnetic field by $B = \mu_o H$, in which $\mu_o = 4\pi \times 10^{-7} \frac{V * s}{A * m}$ is the permeability in the vacuum.

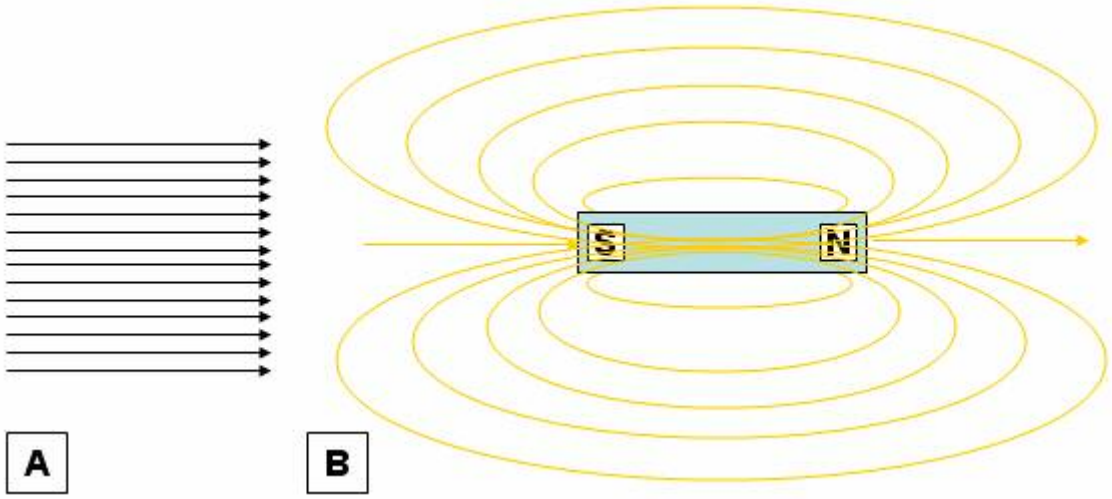

Figure 2.1 (a) Magnetic field lines in vacuum. (b) Magnetic field lines within ferromagnetic materials with permeability u greater than 1.

In Figure 2.1(b) permeability of air μ_o is replaced by the permeability of the material u, which is defined as the ratio of the magnetic flux B in the material and the external

magnetic field H. Hence a relative permeability μ_r can be defined as the ratio of u to μ_o. The relationship between the susceptibility and the relative permeability is

$$\mu = 1 + \chi \tag{2.3.1}$$

in which χ is the susceptibility and it is defined as

$$\chi = \frac{M}{H} \tag{2.3.2}$$

Since the medium shown in Figure 2.1(b) has higher permeability than that of air u_o, which suggests that magnetic field has tendency to immerse in medium with higher magnetic permeability. When an external magnetic field exits inside a material, it gives rise to the induced magnetic flux B and magnetization M due to the magnetic field which have to be taken into account, and the resultant magnetic flux is

$$B_{net} = \mu_o (H + M) \text{ or} \tag{2.3.3}$$

$$B_{net} = \mu_o \mu_r H \tag{2.3.4}$$

by substituting M as a function of χ[1,(20)], where u_o is the permeability of air and u_r is the permeability of magnetic medium. By substituting M as a function of Bnet and H in (2.1.3) into (2.1.2) and doing some manipulation one can obtain the following expression

$$\mu_r = \frac{\chi}{\mu_o} + 1 \tag{2.3.5}$$

where χ is the magnetic scusceptability, μ_o is the permeability of air and μ_r is the permeability of magnetic medium.

Based on the simple mathematical treatment above one can recognize that magnetic materials can be classified according to its relative permeability and susceptibility which reveals the difference among magnetic materials, and such differences can be explained in terms of the atomic structure and the behavior of such structure. Electrons of an atom give rise to the magnetic momentum due to their axis spins and orbital processing. When putting atoms together the influences of the individual magnetic momentum of atoms are coupled, and the net result of the interaction can view as domains. There are some commonly known magnetic materials, namely, diamagnetic, paramagnetic, antiferromagnetic, ferrimagnetic, ferromagnetic materials, and the properties of these materials are shown as in table 1.1.

Table 2.2 Magnetic property of various kinds of materials.[32]

Category	$\frac{\chi}{u_o}$	Examples
Ferromagnetic	10^{7} to 10^{2}	Ni, Fe, Co, NiFe, NdFeB
Ferrimagnetic	10^{4} to 10^{1}	Fe_3O_4, ferrites, garnets
Antiferromagnetic	Small	MnO, NiO, $FeCO_3$
Paramagnetic	10^{-7} to 10^{-6}	Al, Cr, Mn, Pt, Ta, Ti, W
Diamagnetic	-10^{-6} to -10^{-3}	Ag, Au, C, H, Cu, Si, Zn
Superconducting	-1	$YbBa_2Cu_3O_x$

Diamagnetic materials exhibits negative values due to the fact that its orbital and axis momentum are cancelled and a magnetization rises in a direction opposite to the applied magnetic field as can be seen in figure 2.1a.

Paramagnetic and ferromagnetic materials on the other hand have positive values and the positive values suggest the potential for these materials to enhance and concentrate the magnetic flux inside the materials. Magnetic momentum of paramagnetic materials as depicted in figure 2.1b is fairly random which means there is resistance to the magnetization of the materials, and the resistance or magnetic anisotropy explains the smaller value for paramagnetic materials. Ferromagnetic materials shown in figure 2.1c have a strong presence of magnetic momentum even without the applied field and this explains the large value for its $\frac{\chi}{\mu_o}$ ratio. Magnetic materials are also classified as soft and hard. Soft materials can easily be magnetized and demagnetized by an external field; on the other hand the built-in magnetization of hard materials is very strong, therefore, it exhibits permanent magnetization. In the next sub-section, a detailed magnetic structure and its behavior is given.

2.3.2 Magnetic Anisotropy and Magnetic Domain

Magnetic anisotropy is analogous to the resistance to the electric current and plays a big role in magnetization because it influences the shape of hysteresis curve which governs the magnetization characteristics of the nickel film[33]. Some common causes for magnetic anisotropy are described next.

Crystal anisotropy is a type magnetic anisotropy due to the crystal structure itself. There are many crystalline structures such as cubic, hexagonal, tetragonal, and many more, and nickel is a metallic material of cubic structure. In fig. 2.2 magnetization curves and magnetization vectors along easy, medium, hard axes are given.

Magnetization vectors in the demagnetized state are along the easy axes <111>. The crystal anisotropy rises when the magnetized vectors try to align themselves with the external magnetic field because energy must be stored inside the material when its magnetic characteristics are altered by the external means.

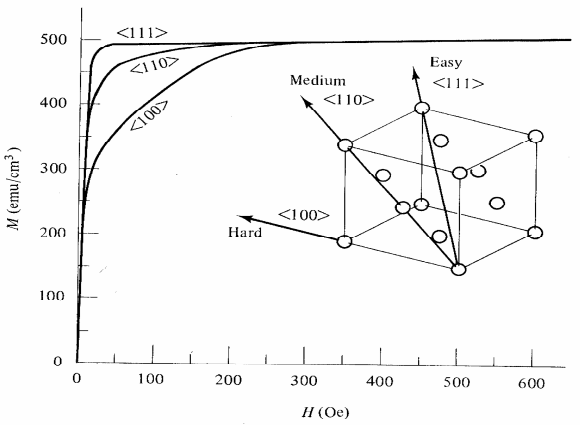

Figure 2.2 Magnetization information in a simplified material structure[34].

Also clearly indicated by the magnetic curves, crystalline directions along <110> and <100> require higher magnetic field to obtain the magnetization than crystalline direction <111>. The anisotropy energy for cubic structure is[34]

$$E = K_o + K_1(\alpha_1^2\alpha_2^2 + \alpha_2^2\alpha_3^2 + \alpha_3^2\alpha_1^2) + K_2(\alpha_1^2\alpha_2^2\alpha_3^2) + ... \qquad (2.3.6)$$

K_o can be neglected since it is not related to angle θ away from the easy axis, $K_1 = -0.5$ and $K_2 = -0.2$ with unit of $10^5 \frac{ergs}{cm^3}$ are anisotropy constants for Nickel, α_1, α_2, and α_3 are numerical values corresponding to angle θ away from the easy axis. The approximated anisotropy energy as a function of θ is given as[33]

$$E = K_1(\sin\phi)^2 \tag{2.3.7}$$

where ϕ is the angle of the magnetization vector away from easy axis.

Shape anisotropy is usually considered when its structure is amorphous, and it has to do with the demagnetizing field under the absence of the external field.

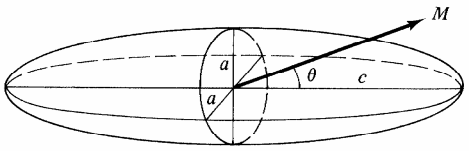

Figure 2.3 The demagnetization field within a sheroid shape material[34]

Fig. 2.3 give a magnetic material with spheroid shape. The magnetized field M shown in fig. 2.3 suggests that different shapes have different degree of magnetization along different axes according to its distinct shape. The energy of shape anisotropy can be expressed as[34]

$$E = \frac{1}{2} N_d M^2 \tag{2.3.8}$$

N_d is the demagnetizing factor calculated based on the geometry of the given material[35].

Magnetostriction is a phenomena under which the magnetic material is under tensile or compressive strength due to the external means such as temperature, pressure, magnetic field, and etc…… Stress anisotropy is related to magnetostriction in the way that it is the energy under the mechanical strength applied to the material sample. The stress anisotropy energy is actually related to crystal anisotropy by the fact that both types of energy are due to the orbit-spin coupling. Therefore, (2.1.9) is applicable to describe

the stress anisotropy with an additional factor σ for the stress imposed on the material. An approximated form for the stress anisotropy is[34]

$$E = (\frac{3}{2}) \cdot \lambda \cdot \sigma (\sin \phi)^2 \qquad (2.3.9)$$

$\lambda_{100} = -46$, $\lambda_{111} = -24$ have unit of 10^{-6} are the magnetostriction factors for nickel. The total anisotropy energy for nickel is superposition of the all the energy described above. With some mathematical approximation and manipulation one can come up with an expression for Etotal[36]

$$E_{total} = (\frac{1}{2}) K_{fotal} \cos(2\phi - 2\delta) \qquad (2.3.10)$$

K_{total} is the overall effective anisotropy constant, ϕ is the angle measured from the magnetization vector to a reference direction, and δ is the angle measured from the overall free axis to a reference direction.

The magnetic domain's micro structure and its behaviors under magnetization is critical to understand the processes of magnetization which leads to changes of the magnetic energy in the magnetic materials[34]. Figure 2.4 shows how domains are formed within a piece of magnetic material. Assuming a piece of material has natural magnetization ands the north pole and south pole are formed subsequently as shown in Fig. 2.4a. Because of the natural tendency to reduce the total magnetostatic energy inside the material a single domain is subdivided into several domains. If a single domain is divided into half, then each sub domain is one half of the original energy as shown in part b and one fourth of the original energy if it is divided into four parts as shown in part c.

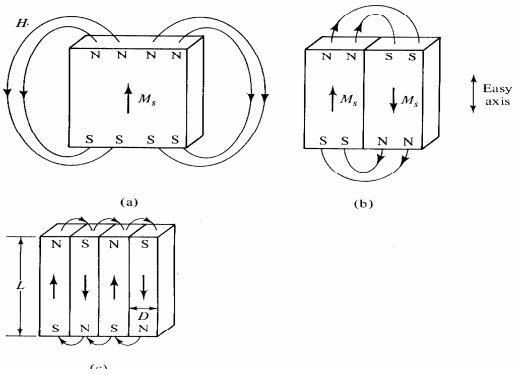

Figure 2.4 Formation of domains within a piece of magnetic material[34].

Also, as one can observe from the figure the divided domains bring the north pole and south pole close together and reduce the magnetic permeation in the air. However the division of a single domain cannot go on indefinitely because each division gives the formation to a boundary which adds energy to the system. In the other words the total boundary energy must be less than the total magnetostatic energy. Fig. 2.5 gives a basic domain structure for the cubic crystals such as nickel and iron. In the domain of cubic crystals the triangular closure domains serve as paths to complete the magnetic loop, and since there are three or four easy axes in the domain of cubic crystals only qualitative analysis is given because a quantitative analysis is rather complicated.

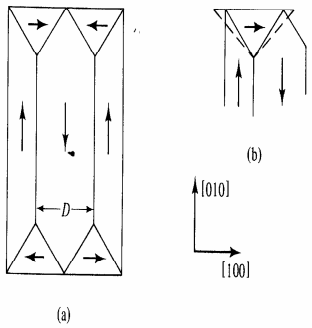

Figure 2.5 Domain structure of cubic structure material[34].

The microstructure and motions of the domain walls between domains plays an important role in the magnetization processes. The classification of domain walls is based on the direction of neighboring magnetic moments: 180^o when two neighboring vectors are anti-parallel, non-180^o when two are parallel, and 90^o when two are perpendicular to each other. Fig. 2.6 delineates the microstructure from one domain to another via a domain wall for the 180^o neighboring magnetic moments. The domain wall is the transition region between two domains and there are certain angle difference between each subsequent magnetization vector. The anisotropy energy per unit area of the domain wall of the magnetization vector has the tendency to reduce length of the wall, and it is defined as

$$\gamma_1 = KNa \tag{2.3.11}$$

where K is the anisotropy constant, a is the length of the cubic structure, and N is the number of atoms in a row within the wall. $\delta = Na$ is the thickness of the wall.

This is the reason for the storage of the anisotropic energy under the influence of the external field, which cause the magnetization of the nickel film. The exchange energy on the other hand tends to increase the length of the wall for a smaller subsequent angle difference, and it is defined as

$$\gamma_2 = \frac{J*S^2*\phi^2*N}{a^2} \tag{2.3.12}$$

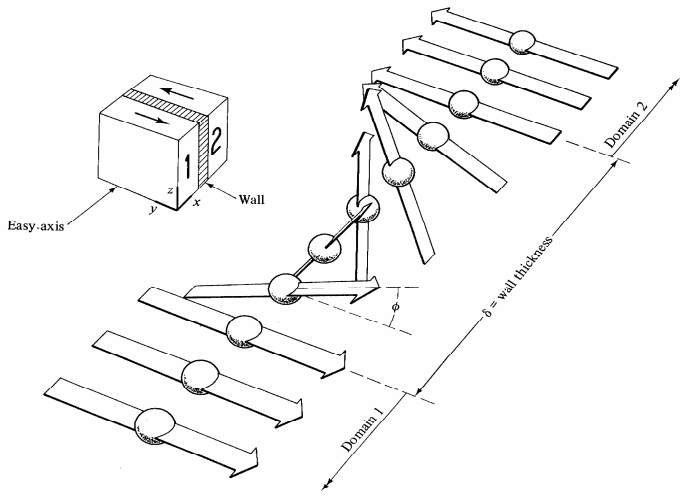

Figure 2.6 Transition of magnetic vectors from one domain to anther[34].

J is the exchange integral which is used to calculate the exchange effect, S is the spin momentum. The competition between the anisotropy energy of the magnetization vectors and the exchanged energy between two domains due to the coupling of the magnetic moment gives a certain limit of the thickness of the wall. The total energy in the 180° wall for $\phi = \frac{\pi}{N}$ is therefore the sum of γ_1 and γ_2, and one can obtain the smallest thickness to be

$$\delta = \frac{J * \pi^2}{4Ka} \tag{2.3.13}$$

in which $J = 0.3kT_c$, $S = \frac{1}{2}$, K is the boltzmann's constant and T_c is the curie temperature for iron and nickel. Once the microstructure is understood motion of the domains and the domain walls under the influence of the magnetic field can be illustrated subsequently by fig. 2.7.

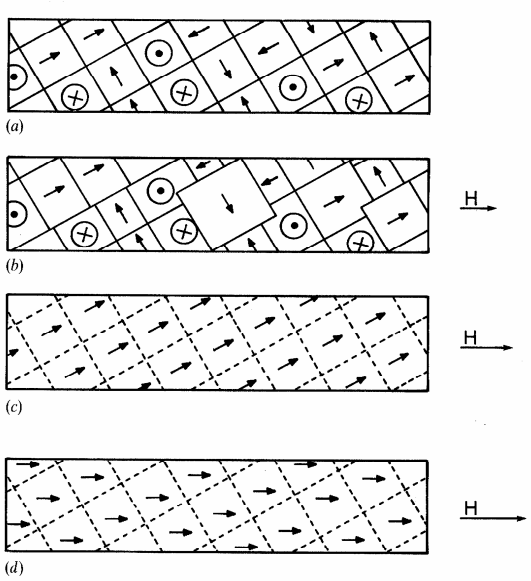

Figure 2.7 The processes of magnetization by the external magnetic field[35]

It is mentioned in the previous sections that ferromagnetic materials such as nickel and iron exhibit certain degree of magnetization in its demagnetized state as shown in figure 2.7a. Part (b) of Fig. 2.7 illustrates that when the ferromagnetic material is under the influence of the low field the region of domains with the direction of magnetic momentum opposite to the external magnetic field shrinks because some magnetization vectors are aligned to the domains, which are in the direction of the external magnetic field. And one can make observation on part b of Fig. 2.7 such that some domains aggrandize in size and some shrink as result of the domain and wall movement. Part c of Fig. 2.7 shows that when the external magnetic field increases till all domains have the magnetization vectors in the same direction although not necessarily parallel to the field, and this condition is termed as technical saturation magnetization. The further increase in the magnetic field align all the magnetization vectors as shown in part d. Although the magnetization processes of materials can be explained by the microstructure of the

domains, magnetic anisotropies rise during the processes of magnetization. The magnetic anisotropies need to be further investigated in order to fully understand the motion of micro-magnetic devices.

2.3.3 Consideration of Mgnetic Force and Torque

Material properties are important factors when comes to develop an actuator with high speed and large displacement. As mentioned in the introduction chapter the idea of magnetic actuation has been utilized for detection and motion movement. Most of the theory developed for the magnetic actuation is based on the idea of the magnetic compass. The magnetic compass is composed of a metal magnetized by the lodestone which is type of a magnetic rock called magnetite. The magnetic compass is used to find directions because of its tendency to align its needle with the magnetic field of the earth, and this idea can be easily demonstrated by detecting the direction of the magnetic field around an electrical wire with a current passing through. A mathematical description of the mechanical torque of the magnetized needle under the influence of the external magnetic field is

$$\tau = \left| m_{ni} \times B_{ext} \right| = V_{ni} M_{ni} H_{ext} \sin(\xi - \theta) \tag{2.3.14}$$

V_{ni} is the volume of the nickel film, M_{ni} is the magnetization per volume, and H_{ext} is the applied magnetic field. For the fiber optical scanner we are working on an optical fiber is always attracted to the electromagnet which produces non-uniform magnetic field, hence, an alternative description is required.

Unlike the torque being generated in the case of magnetic compass, the translational force is generated by the interaction of the external magnetic field gradient and the magnetization due to the field itself. The translational force based on Biot-Savart's law is can be expressed mathematically as

$$F_{mag} = (M(H) \cdot \nabla)B \tag{2.3.15}$$

where M is the volume density of magnetization moment, H is the external magnetic field, and B is the external magnetic flux. From the expression we can also see that magnetic permeability plays a dominant factor in maximizing magnetic force. The category of ferromagnetic materials shows the high susceptibility, which is directly related to permeability. More important, not all ferromagnetic materials are suitable for constructing an actuator because of the hysteresis energy of the material itself. Herein another property that characterizes material called hysteresis curve is introduced. Figure 2.8 shows hysteresis loops for magnetically soft and hard materials. On one hand, with magnetic hard materials, the hysteresis loop is merely square, which means BH product is large. The consequence of large BH product is the large stored magnetic energy, which is difficult to remove, and this type of magnet is often called permanent magnet. On the other hand, soft or un-poled magnetic materials such as nickel and iron have a rather small BH product and steep curve, which implies high magnetic permeability. Likewise, low magnetic coercivity is critical for fast scanning application because the remnant magnetic field can be erased readily by low strength magnetic field.

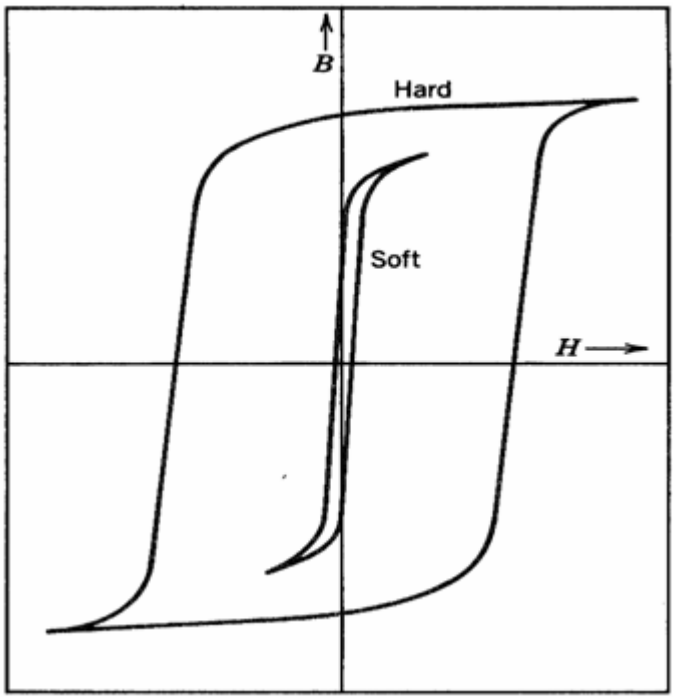

Figure 2.8 Hysteresis curve for magnetically soft and hard materials.[21]

Moreover, high magnetization can be induced by a relatively smaller external magnetic field in soft materials than hard material.

2.3.4 Contemporary Magnetic Optical Scanners and Their Applications

Currently magnetic actuators and sensors have been developed for applications in magnetic field sensing for automotive applications, current sensing, magneto-metering, biomedical applications[20-23]. Magnetic sensors are well known for their use in automobile navigating. For automotive applications, magnetic sensors offer advantages such as contactless and wear-free quantification of mechanical motion. Just in the last few years, researchers have used magnetic sensors for measurement of wheel speed, control of vehicle dynamics, engine control for speed and position. Magnetic sensors also found as a crucial component for current sensing in power electronics as the trends of power electronics go towards high power density, high functional integrations, and low

cost per wattages because magnetic sensors provide the necessary feedback control mechanism in the power electronics for uninterrupted and versatile operations. The state of the art for AC current sensing in power electronics is up to 100 KHz. Micromechanical system based magnetic field sensors have draw attentions these days since the intrinsic parasitic power lost in conventional semiconductor based magnetic sensors are evaded. A torsion beam with a piece of permanent magnet can act as a magnetic field sensor has been reported, and mechanical response to external magnetic field as small as 200 nT was demonstrated.

Fiber optical systems based magnetic and electromagnetic sensors and actuators have been invented by several groups[24-27], and they found applications in magnetic field sensors and 2-D or 3-D optical signal switching. Toshiyoshi et al. demonstrated optical fiber switching system based on electromagnetic torsion mirrors using permanent magnet capable of 90^{o} mirror rotation[25], but it requires 12 watts of power consumption because of the large coil diameter. An electromagnetically actuated mirror arrays for 3-D optical switching developed by Bernstein et al. can deflect about 10^{o} with low power consumption of 124 μW; however, the mirror arrays require eight fabrication steps to be accomplished[26]. Nagoaka et al constructed an electromagnetic optical fiber switch with permanent magnet and mesh coils[24]. The mesh coils are wrapped around an ultra-light micro-magnetic alloy pipe which contains a movable single mode fiber inside a sleeve, and permanent magnets are fixed on the ceramic half-cylindrical ferrules with one on the upper side and the other on the lower side outside of the sleeve. When electric current is pumped into the mesh coils the movable optical fiber can move up and down as an optical switch. This device could pose some challenges for some applications when

minimal dimensions are critical requirement. Deeter et al. reported an optical fiber based magnetic field sensor with high sensitivity using iron garnets[27]. The magnetic sensor demonstrated the detection of minimal magnetic field of $\frac{1.4\,pT}{\sqrt{Hz}}$ at 1 KHz. In the next section, a theoretical treatment on oscillating optical fiber is given to serve as support for the experimental sections.

2.3.5 Theory and Physical Principles of an Oscillating Optical Scanner

Two types of magnetic forces are generally being utilized in magnetic actuation. One is the induction of magnetic force analogous to the mutual attraction of two magnets, and the other is the torque induced by the interaction of magnetic fields as in the case of a magnetic compass, which operates when the earth's magnetic field interacts with lodestone, which is a permanently magnetized medium. Type of forces being employed depends on the nature of magnetic materials and ways of implementation. Magnetically soft materials such as Ni, Fe, NiFe are often used for producing attractive magnetic forces. Permanent magnets such as NdFeB and magnetic pre-poled soft materials are used to produce torques. In order to produce attractive translational forces un-poled nickel (Ni) powder is used for our device. Figure 3 illustrates the physical bending motion of the magnetic gel coated optical fiber under the application of magnetic field. In Fig. 2.9a without the external magnetic field the magnetic vectors of magnetic domains are in random phases, and the fiber optic scanner has no displacement motion. When the magnetic field is applied as in the case of Fig. 2.9b the fiber optic scanner starts to bend, and the magnetic vectors of magnetic domains are trying to align themselves. Fig. 2.9c shows that with the continual increase of magnetic field the fiber optic scanner

bends further when all magnetic vectors are aligned with the external magnetic field, which is the ultimate limit of actuation and is termed as magnetic saturation.

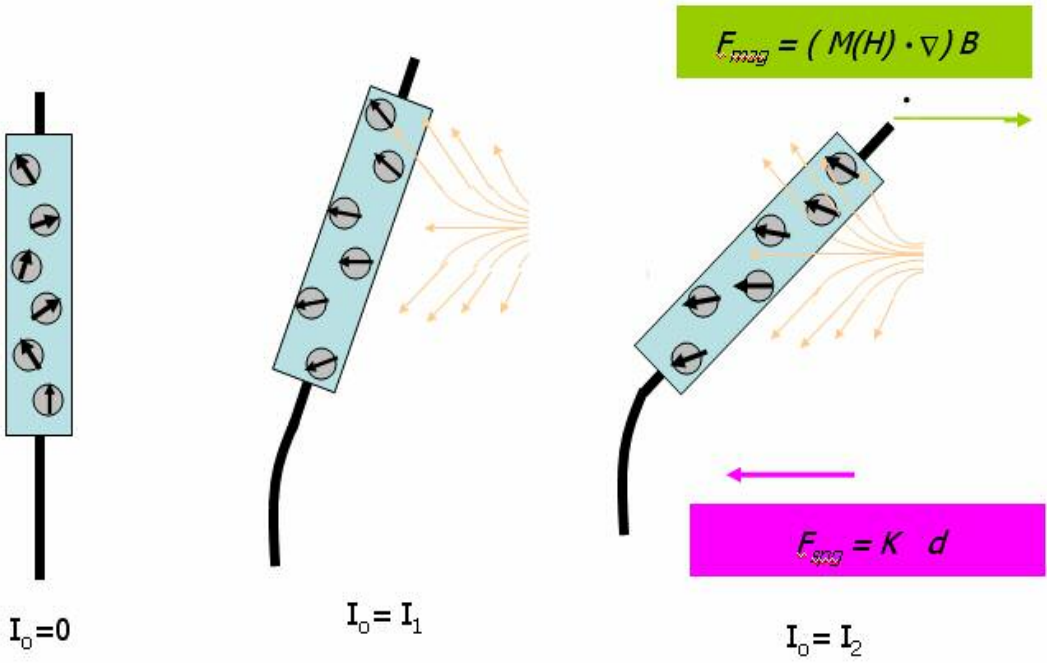

Figure 2.9 Motion of magnetic moment vectors under the influence of external magnetic field.

By actuating magnetically, mechanical bending force is induced. In the next following sub-sections, dynamic analysis of magnetic actuated optical fiber is followed by the static analysis. In static analysis, the derivations of static magnetic and mechanical forces are shown and the relationship between forces is described. In the dynamic analysis, the equation for calculating the resonant frequencies is derived analytically.

2.3.6 Mechanical Analysis

The mechanical characteristics of an optical fiber need to be considered because the mechanical properties of the material give rise to its mechanical force, and the restoring mechanical force retards the magnetic translational force. The shear stress due

to material deformation plays an important role In the following the stiffness and first mode resonant frequency are derived analytically[29].

Fi

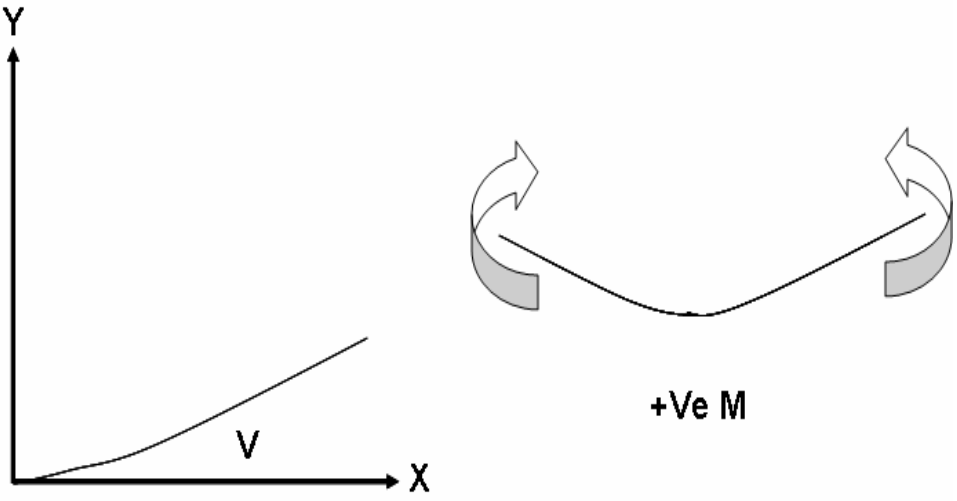

Figure 2.10 Sign conventions of displacement and moment directions.

The relationship of moment curvature is vital in performing mechanical analysis of an optical fiber. For the following mechanical analysis the sign conventions in figure 2.10 adopted. The moment curvature relationship is define as

$$M = EI\frac{d^2v}{dx^2} \tag{2.3.16}$$

Where M is bending moment, E is young's modulus of SiO_2, and v is displacement in y direction. I is the circular area moment of inertia, and it is defined as

$$I = \frac{\pi r^4}{4} \tag{2.3.17}$$

where r is the radius of optical fiber. For the analysis here, let's consider an optical fiber with external force acting at the tip of the optical fiber, which is in figure 2.11.

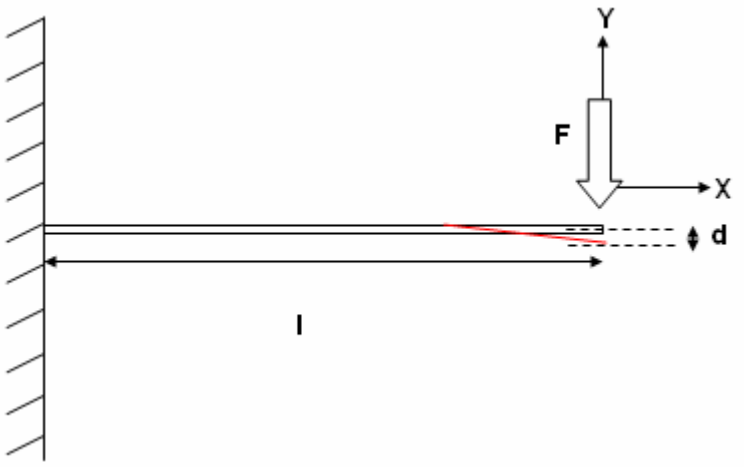

Figure 2.11 An optical fiber under external load.

By the convention shown in figure 2.10, the moment induced by the bending at distance x is

$$M = -F_{sp} * x \tag{2.3.18}$$

were F_{sp} is the mechanical spring force.

With the substitution of Eq. 2.3.16 into Eq. 2.3.18, the expression can be rewritten as

$$EI\frac{d^2v}{dx^2} = -F_{sp} * x \tag{2.3.19}$$

Since displacement v is double differential function, integration is taken as the following

$$\int EI\frac{d^2v}{dx^2} = \int -F_{sp} * x$$

$$EI\frac{dv}{dx} = -\frac{F_{sp}x^2}{2} + C_1$$

Using boundary condition at $x = l$, at which the bending slope is zero,

$$C_1 = \frac{F_{sp} l^2}{2}$$

$$EI \frac{dv}{dx} = -\frac{F_{sp} x^2}{2} + \frac{F_{sp} l^2}{2} \tag{2.3.20}$$

by taking integration of Eq. 2.3.20

$$\int EI \frac{dv}{dx} = \int \left(-\frac{F_{sp} x^2}{2} + \frac{F_{sp} l^2}{2} \right)$$

$$EIv = -\frac{F_{sp} x^3}{6} + \frac{F_{sp} l^2 x}{2} - \frac{F_{sp} l^3}{3}$$

(2.3.21)

by setting x = 0 in Eq. 2.3.20

$$S = \frac{dv}{dx} = \frac{F_{sp} l^2}{2eEI} \tag{2.3.22}$$

likewise, by setting x = 0 in Eq. 2.3.21 the downward displacement can be quantified as

$$v = -\frac{F_{sp} l^3}{3EI} \tag{2.3.23}$$

by rearranging the Eq. 2.3.23,

$$F_{sp} = \frac{3EI}{l^3} v \tag{2.3.24}$$

$$F_{sp} = Kv \tag{2.3.25}$$

where K is the linear spring constant

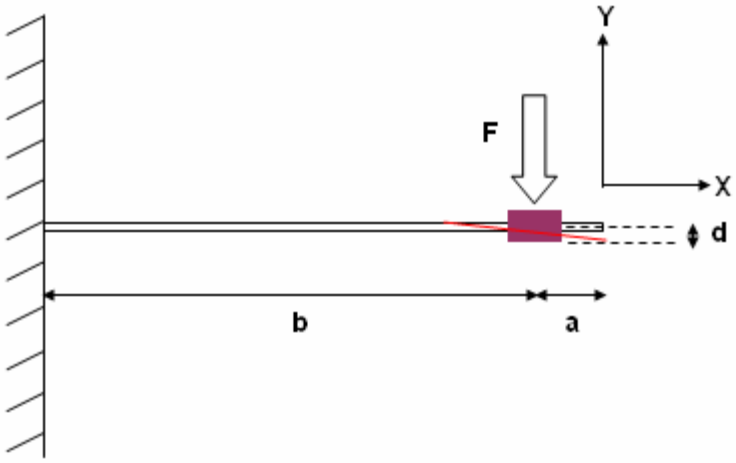

Figure 2.12 Magnetic gel coating incorporated optical fiber under external magnetic force.

Fig. 2.12 shows the situation when magnetic coating is taken into consideration for the behavior of optical fiber motion. The total deflection of the optical fiber, d, is equal to the deflection of an optical fiber due to magnetic force acting at the point B and the multiplication of slope of the optical fiber from B to A and the distance of the point B to the tip A. With Eq. 2.3.22 and Eq. 2.3.23,

$$d = \frac{F_{sp} b^3}{3EI} + \frac{F_{sp} a^2}{2EI} a \tag{2.3.26}$$

by rearranging 2.3.26, the final expression for mechanical spring force is

$$F_{sp} = \frac{1}{\left(\frac{b^3}{3EI} + \frac{a^3}{2EI} \right)} d = Kd \tag{2.3.27}$$

2.3.7 Magnetic Analysis

Magnetics is a branch of science concerns how magnetic materials react to an external magnetic field. More specifically how magnetization property varies due to the

difference in crystal structure, chemical composition and external influences such as heat and mechanical pressure. Magnetization of magnetic materials plays a vital role in inducing magnetic force. As was mentioned, nickel is a ferromagnetic material with high magnetic permeability, which is due to the alignment of domains of magnetic moment along the direction of external magnetic field. In this sub-section, magnetic force formulation is reviewed and derived[30]. Let's consider a piece of magnetic materials with the shape of cylindrical shell shown in figure 2.13. Equal magnitude and opposite polarity of the density of magnetic poles $\rho = \mu_o M$ appear at both ends of area a_d when subjected to an external magnetic field. Volume of ferromagnetic coating is

$$\delta V = a_d d \tag{2.3.28}$$

The force experienced by the above volume is

$$-H_o \rho_s a_d + (H_o + \delta H_o)\rho_s a_d = \delta H_o \rho_s a_d \tag{2.3.29}$$

where δH_o is the change in magnetic field along the direction of d, thus

$$\delta H = (d * \nabla) H_o = \left(\frac{d}{M}\right)(M * \nabla) H_o$$

and the density of magnetic force is given as

$$MagneticForcDensity = \mu_o (M \cdot \nabla) H_o \tag{2.3.30}$$

In Eq.2.15 2.3.30, $m = \mu_o M a_d d$

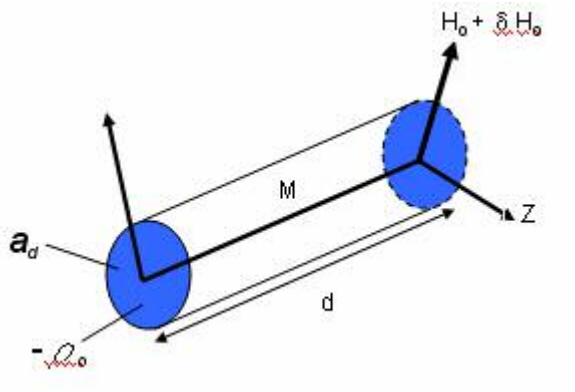

Figure 2.13 Model of magnetic dipole moment distribution for theoretical analysis.

For constant field approximation

$$F_{mag} = \mu_o \cdot M \cdot V \cdot \nabla H_o \tag{2.3.31}$$

$$F_{mag} = \mu_o \cdot M \cdot V \cdot (\frac{dH_o}{dz} + \frac{dH_o}{dx} + \frac{dH_o}{dy}) \tag{2.3.32}$$

For a rough estimation of the magnetic force, the magnetic field gradient in x and y direction is neglected. Hence the magnetic force is

$$F_{mag} = \mu_o \cdot M \cdot V \cdot \frac{dH_o}{dz} \tag{2.3.33}$$

2.3.8 Static Analysis

With magnetic coating coated at the tip of an optical fiber, the translational motion of optical fiber can be induced when a D.C. magnetic field is applied to the magnetic coating. For static actuation, for the optical fiber to remain in a particular position when actuated, the magnetic force and spring restoring force must be at equilibrium as

$$F_{spg} + F_{mag} = 0$$

$$F_{mag} = \mu_o \cdot M \cdot V \cdot \frac{dH_o}{dz} = Kd \tag{2.3.34}$$

where linear spring constant K is given in Eq. 2.3.27. By rearranging 2.3.24 The displacement d can be expressed as

$$d = \mu_o \cdot M \cdot V \cdot \frac{dH_o}{dz}\left(\frac{b^3}{3EI} + \frac{a^3}{2EI}\right) \tag{2.3.35}$$

Comparison of theory and experiments for displacement d with optical fiber length 4.2cm and 5.2cm is done by Dhaubanjar et. al.[28].

2.3.9 Dynamic Analysis

The dynamic motion of device has its importance in terms of power consumption, speed, and displacement. At the state of natural resonant frequencies, oscillating devices require minimum amount of power to operate as compared to its static motion. By tailoring the dimensions of the oscillating device, various speed can be achieved with providence of enough force. In this section, the derivation of fundamental mode resonant frequency is done using Rayleigh's method, which states that the kinetic energy is equal to potential energy[31].

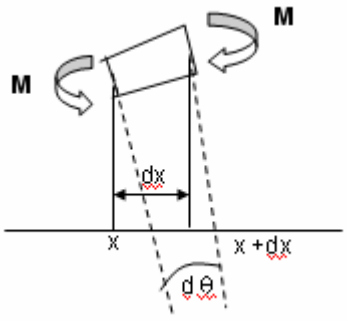

Figure 2.14 Graphical illumination of potential energy distribution in a beam element.

Figure 2.14 shows the potential energy moment diagram for a finite beam element. From strength of materials, the potential energy of a differential element is definite as

$$dPE = \frac{M^2}{2EI} dx \tag{2.3.36}$$

by substituting 2.3.16 into 2.3.36,

$$dPE = \frac{EI}{2}(\frac{d^2y}{dx^2})^2 dx$$

by integrating the above expression

$$PE = \frac{EI}{2}\int_0^l (\frac{d^2y}{dx^2})^2 dx \tag{2.3.37}$$

Classically, kinetic energy is define as

$$KE = \frac{1}{2}mv^2$$

or $\frac{1}{2}(\mu_1 dx)(vw)^2$ where u_1 is the total mass of various elements, v is y displacement, and w is circular frequency.

for a choosen form of v

$$KE = \frac{1}{2}u_1 w^2 \int_0^l y^2 dx \tag{2.3.38}$$

Quarter cosine wave form is used to describe the dynamic motion of a cantilever, an optical fiber for the case of this work. The curve of Rayleigh shape for a cantilever is shown in figure 2.15. The expression of a quarter cosine wave is

$$y = y_o(1 - \cos\frac{\pi x}{2l}) \tag{2.3.39}$$

by substituting 2.3.39 into 2.3.38 and 2.3.37,

$$PE = (\frac{\pi^4}{64}) \cdot (\frac{EI}{l^3}) y^2{}_o \tag{2.3.40}$$

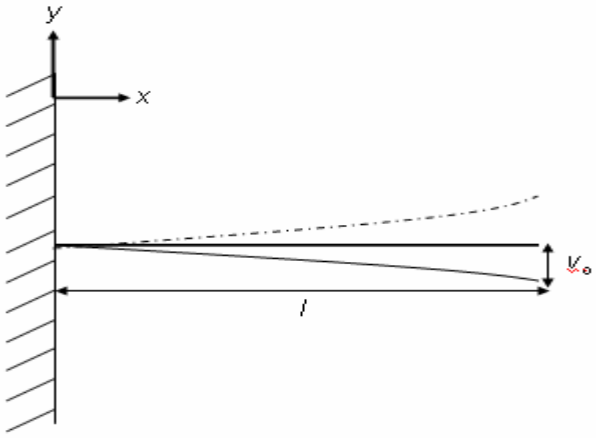

Figure 2.15 A quarter cosine wave of Rayleigh curve estimation for a cantilever.

$$KE = u_1 w^2 y_o{}^2 l \cdot (\frac{3}{4} - \frac{2}{\pi}) \tag{2.3.41}$$

since magnetic gel is also part of the entire device, its kinetic energy has to be added to the kinetic energy of the optical fiber and it is

$$KE_{mag} = \frac{1}{2} M_g w^2 y_o{}^2$$

$$KE_{total} = \frac{1}{2} M_g w^2 y_o{}^2 + u_1 w^2 y_o{}^2 l \cdot (\frac{3}{4} - \frac{2}{\pi}) \tag{2.3.42}$$

$$m_f = u_1 l \tag{2.3.43}$$

by equating 2.3.42 and 2.3.40 with substitution of 2.3.43

$$\frac{1}{2} w^2 y_o{}^2 (M_g + 0.23 m_f) = \frac{\pi^4}{64} \frac{EI}{l^3} y_o{}^2$$

$$w^2 = \frac{3EI}{l^3 (M_g + 0.23 m_f)} \tag{2.3.44}$$

the final expression for fundamental mode resonant frequency is

$$f = \frac{1}{2\pi} \sqrt{\frac{3EI}{l^3 (M_g + 0.23 m_f)}} \tag{2.3.45}$$

2.3.10 Magnetic Characterization

In the previous sub-sections, magnetic theory was given as an introduction to illustrate a variety of magnetic materials and their properties. There are several ways that we can characterize magnetic materials. One way is by the magnitude of magnetic susceptibility, which is related to magnetic permeability with an addition of numerical one. Another way the magnetic material is categorized by its magnetic hysteresis curve. In this section the methods and experimental data for magnetic field measurement and magnetic hysteresis curve measurement are illustrated and shown.

The rise of motion of magnetic gel coated optical fiber is due to magnetization of nickel particles by the magnetic field gradient. The magnetic field gradient induced by a commercial electromagnet cannot be simulated because the device parameters are unknown; therefore, the exact magnetic field gradient distribution cannot be calculated and quantified. In order to quantify magnetic field gradient, an average of magnetic field gradient is measured using gaussmeter (F.W. BELL 5080 Gaussmeter). The experimental setup for magnetic field measurement is shown in figure 2.16.

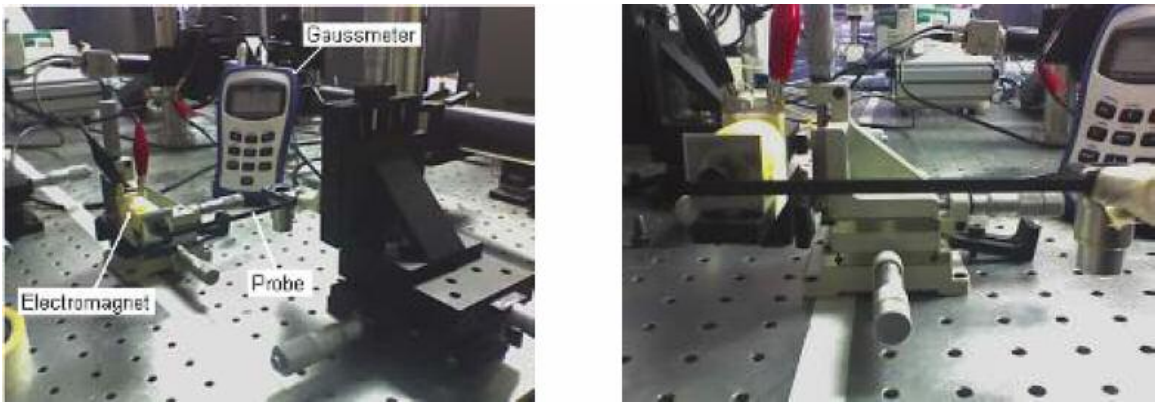

Figure 2.16 Experimental setup for the measurement of average magnetic field strength.

In order to standardize experiments for characterizing the magnetic fiber optic devices, the distance between electromagnet core and optical fiber needs to be set. Figure 2.17 shows three plots of the average magnetic field strength as a function of input electric current. Based on the figure, as the electric current gets higher the iron core of electromagnet tends to get saturated, and another obvious fact is that field strength is higher when the distance between core and hall probe is smaller for a given magnitude of input electric current. Alternating gradient magnetometer (AGM) is used to characterize magnetic hysteresis curve, and a photo of AGM is shown in figure 2.18. The working principle of AGM is the following.

Samples smaller than 2mm by 2mm is used and attached to a sample holder, and the sample holder is a part of rotary piezoelectric bar. The sample holder is in between two electromagnetic coils. External magnetic field is first measured by a hall probe. The sample is rotated due the influenced of the external field. The piezoelectric bar is then rotated and obtained the voltage signal due to piezoelectric effect. A hysteresis curve is then plotted by a computer. An example of magnetic hysteresis curve done on a sample with nickel powder based materials is delineated in figure 2.19.

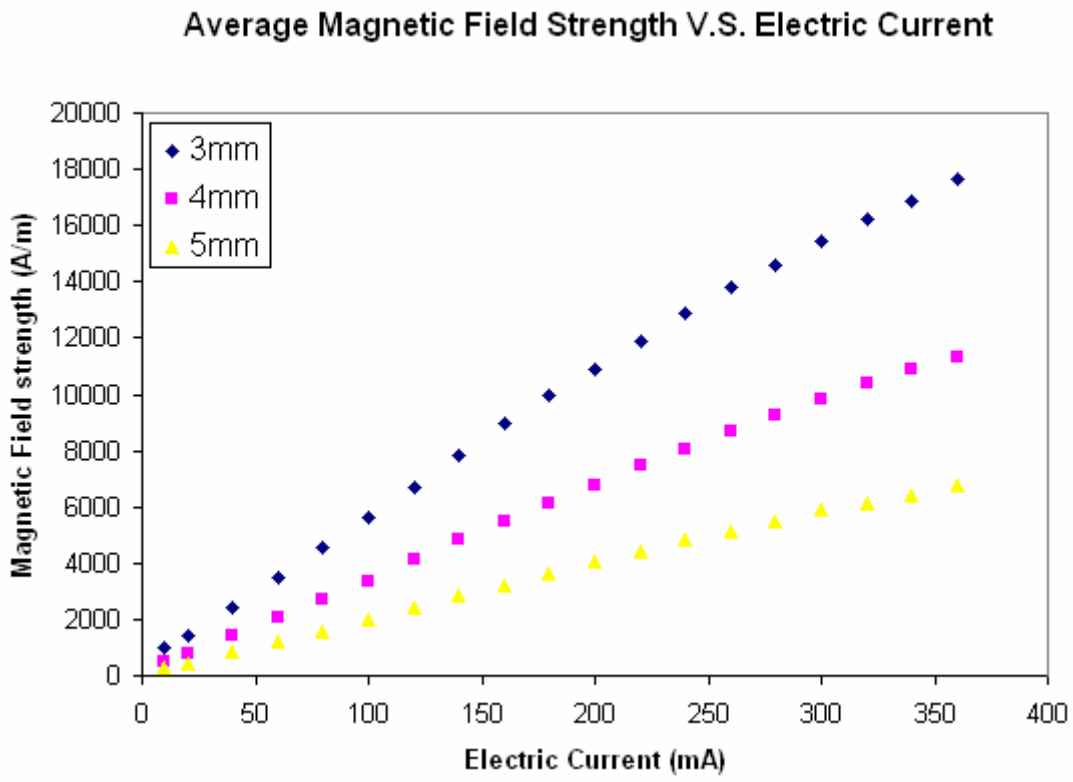

Figure 2.17 Average magnetic field strength as a function of input electric current for different distance between magnetic hall probe and the core of electromagnet.

Herein with the hysteresis curve shown, some parameters associated with the curve are introduced. Magnetic remnant flux is the magnetic moment left behind in the magnetic material when external magnetic field is removed. It takes certain magnetic field strength or coercive field strength to remove the remnant flux. To build a fast scanning device, the smaller the coercive field the better. The last parameter is magnetic saturation is a parameter ultimately determines how much magnetic field can apply to a piece of material, so that the material would still give magnetic response.

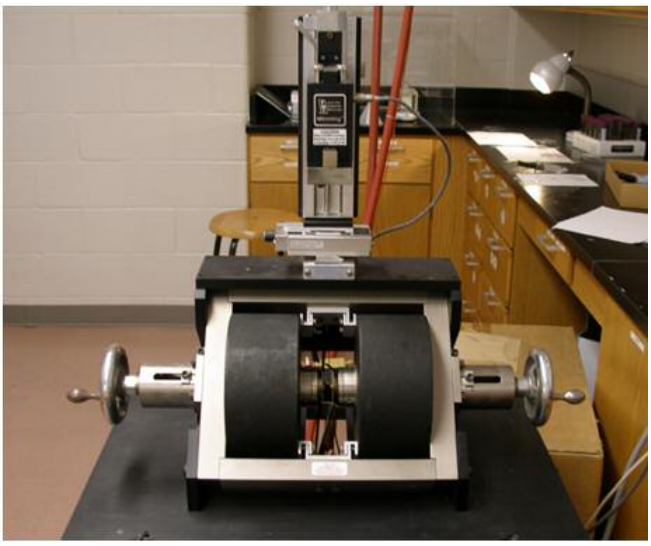

Figure 2.18 Experimental setup of the alternating gradient magnetometer.

In the next section the construction of electromagnetic actuator is delineated from the material and structural perspectives. The potential advantages of the electromagnetic actuator for endoscopic applications are emphasized. Finally, static and dynamic performance data of the electromagnetic actuator are shown to demonstrate the potentials for the targeting application.

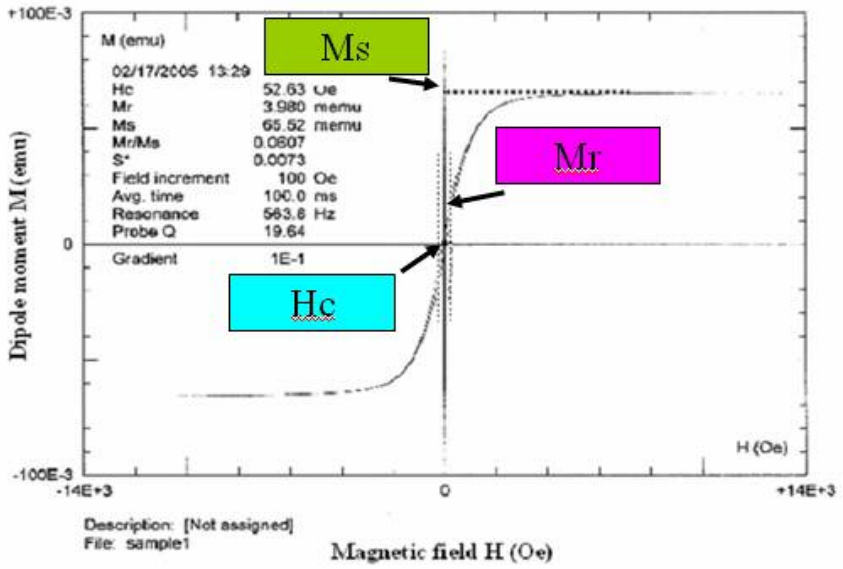

Figure 2.19 Magnetic hyteresis characterization for a sample of nickel powder based material using epoxy as medium.

2.3.11 Magnetic Fiber Optical Scanner

The development of an optical scanner for endoscopic application has the followingrequirement: small dimensions, large scan range and low power consumption. As mentioned in the previous sections optical fiber is an ideal medium for light delivery for its small dimensions and light weight. In the literatures researchers have mounted an optical fiber on top of actuators to perform optical scanning. Rather than doing so, an optical fiber coated with ferromagnetic paint can be translated directly using an external magnetic field source. Figure 2.20 shows a schematic of the electromagnetic fiber optical scanner. The whole electromagnetic scanner is composed of a ferromagnetic paint coated optical fiber and an external electromagnet. An optical fiber coated with magnetic paint can be influenced by external magnetic field.

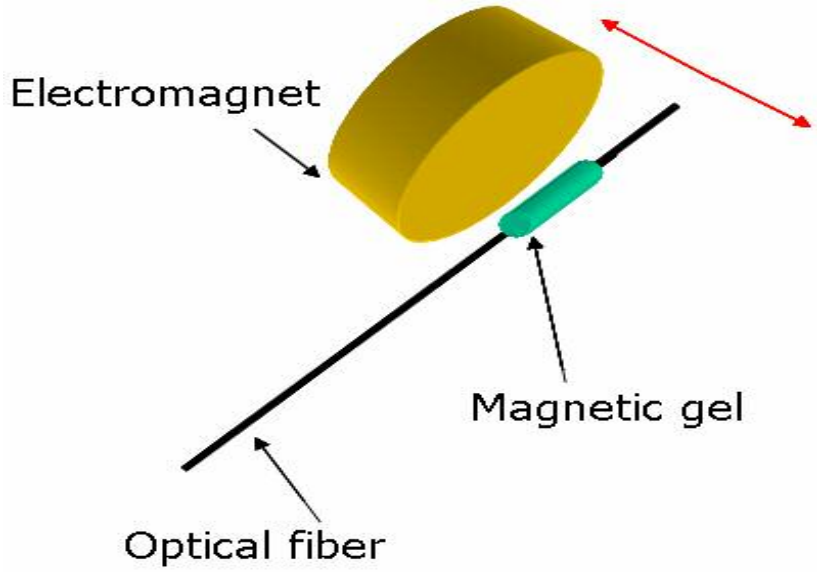

Figure 2.20 The layout of the assembly for the electromagnetic fiber optic scanner

The advantages of the actuation scheme is three-fold: (1) dimensions in tens of μm can easily be inserted in a limited volume, (2) electromagnetic steering without wiring on the

scanner, (3) zero-power consumption. Electromagnetic actuators and sensors require techniques such as electroplating and thermal evaporation to coat magnetic thin film on the device structures. The quality of these films using above techniques are very often critically dependent on temperature, pressure, and the stability of electric current or voltage levels[38]; besides, these techniques can only deposit 2-D structure thin films, and more fabrication steps are required for complicated geometries[39]. One of the key development of the electromagnetic optical scanner is a simple and temperature and pressure invariant fabrication process. Epoxy gel was used as the medium to form a magnetic powder matrix at the very early phase of the development.

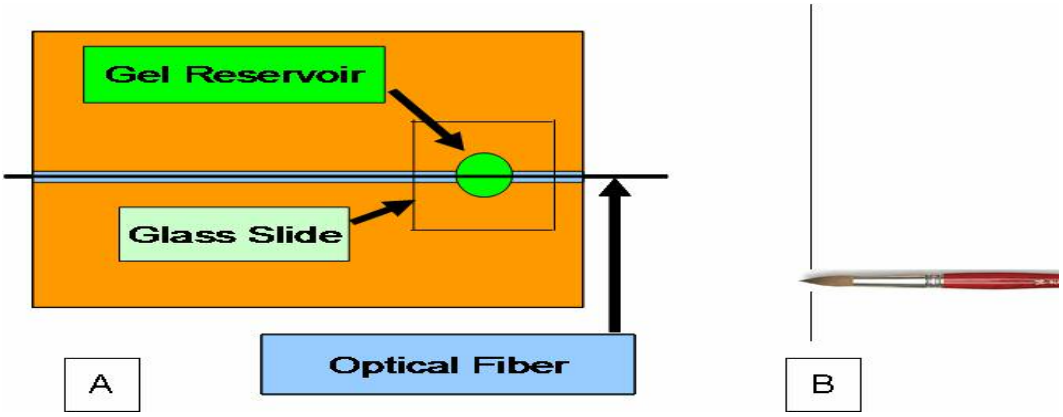

Figure 2.21 Existing coating technique used. (a) A rotary technique. (b) Dip-coating with assistance of paint brush.

Figure 2.21(a) shows the setup for epoxy gel coating. In order to coat an optical fiber with the magnetic gel, an optical fiber is placed in a v-groove trench on an acrylic block with a reservoir along the channel filled with magnetic gel. A glass slide covers the top of the reservoir to confine the magnetic gel and the optical fiber. By rotating the

optical fiber about the axis of its length, a thin film of magnetic gel can then be coated onto an optical fiber; the length of the magnetic gel along the optical fiber is about 5 mm. Because of the non-uniformity of epoxy gel when coated on an optical fiber, a water-soluble paint is used for its lower viscosity. A direct dip-coating with the assistance of paint brush is implemented as shown in Figure 2.21(b). Figure 2.22 shows the microscope images of cross-sectional view of typical coatings using both epoxy gel on the left and water-soluble paint on the right. Better non-uniformity is clearly shown when using water-soluble paint as a medium. In both cases of two different types of medium, 30% and 50% of with 3.5 um-size nickel powder by weight as compared to the mass of the medium are used.

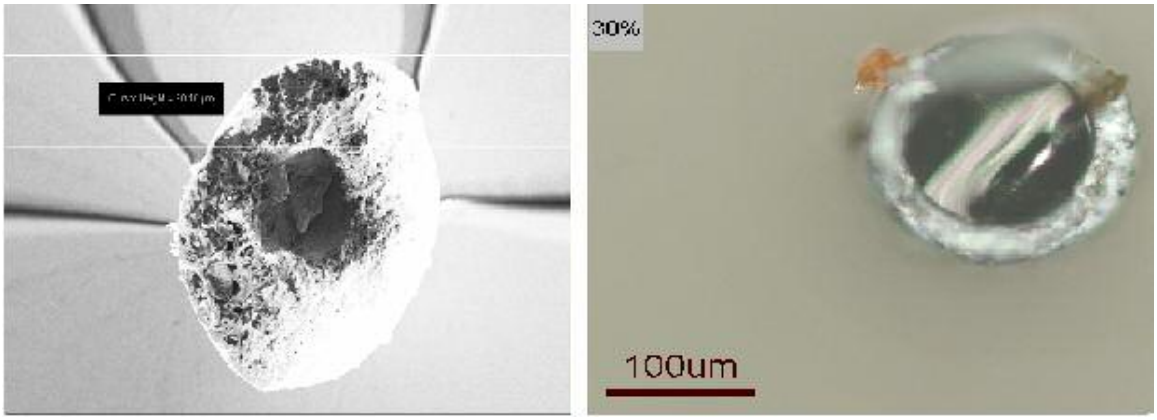

Figure 2.22 Cross-sectional view of coatings using epoxy gel and water-soluble paint. Left figure is an image done with SEM, and right figure is by an optical microscope.

To characterize and compare the magnetic property of material medium made with 30% and 50% nickel powder, experimental magnetic hysteresis curves are plotted and shown in Figure 2.23. The samples based on Ni- powder paint used in these particular experiments are 2.31 mm by 2.31 mm in area and 0.04 mm in thickness.

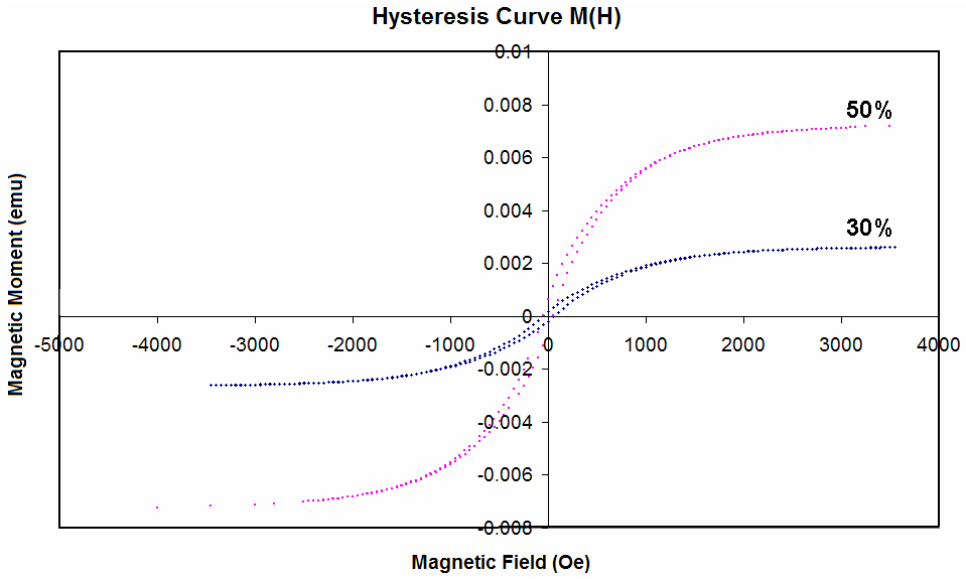

Figure 2.23 Magnetic hysteresis curves for ferromagnetic paint with nickel powder 30% and 50% by weight.

Though the precise permeability cannot be calculated since the exact amount of nickel powder being coated is unknown, the collected data of 50% nickel coating sample illustrates higher magnetization response under a given external magnetic field, and this suggests higher magnetic force and longer scanning range. Since the work is dedicated for dynamic fast scanning, the expression to calculate the natural resonant frequency is given as Eq. 2.3.45

$$F_n = \frac{1}{2\pi}\sqrt{\frac{3EI}{l^3(M_{mag} + 0.23m_c)}}$$

where E, the Young's modulus, is 7.24E10 $\frac{N}{m^2}$ for an silicon optical fiber , l is the length of the actuator, M_{mag} is the mass of the ferromagnetic medium, and m_c is the mass of an optical fiber. In the following section, the static and dynamic characterization is done on

the fiber optic scanner. Figure 2.4 Magnetic hysteresis curves for ferromagnetic paint with nickel powder 30% and 50% by weight.

2.4 Preliminary Performance Results

The fiber optical scanners are characterized using direct butt coupling method. Figure 2.24(a) and (b) shows the diagram of the experimental setup layout and the actual setup. A HeNe laser beam at wavelength of 632.8 nm with optical power of 20 mW is shone onto an objective lens with focal length of 0.5mm which focuses the beam into the fiber optical scanner. With a D.C. or an A.C. electric current applied to an electromagnet with frequency bandwidth of 60 Hz and resistance of 30 ohm, the fiber optical scanner can scan statically or dynamically. The magnetic field strength of the electromagnet at 3 mm away from its magnetic core are measured experimentally by gaussmeter (F.W. BELL 5080 Gaussmeter) The static and dynamic characteristics of the fiber optic scanner are tested by a one-dimensional position sensing device(PSD). To perform a static analysis, a voltage source is applied directly onto the electromagnet, and a current meter is connected in series to monitor the current flowing into the magnetic coils.

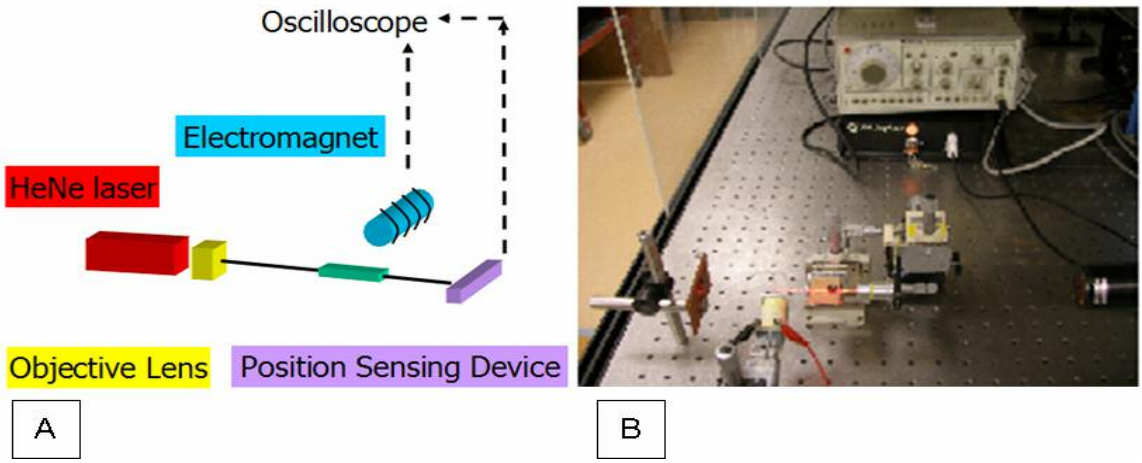

Figure 2.24 (a) Layout diagram of experimental setup. (b) A real experimental setup on an optical bench.

For Static measurement, the currents of the anode and cathode are directly measured using an electronic multi-meter. The scan length is calculated using the ratio of the currents from the anode and cathode. Ultimately, the amount of nickel powder being coated is essential because it determines the maximum of achievable static displacement. Figure 2.25 shows images of the thickness of the coating for optical scanners with both 30% and 50% nickel powder by mass taken using optical microscope. The thickness for 30% and 50% are 30 um and 45 um, respectively.

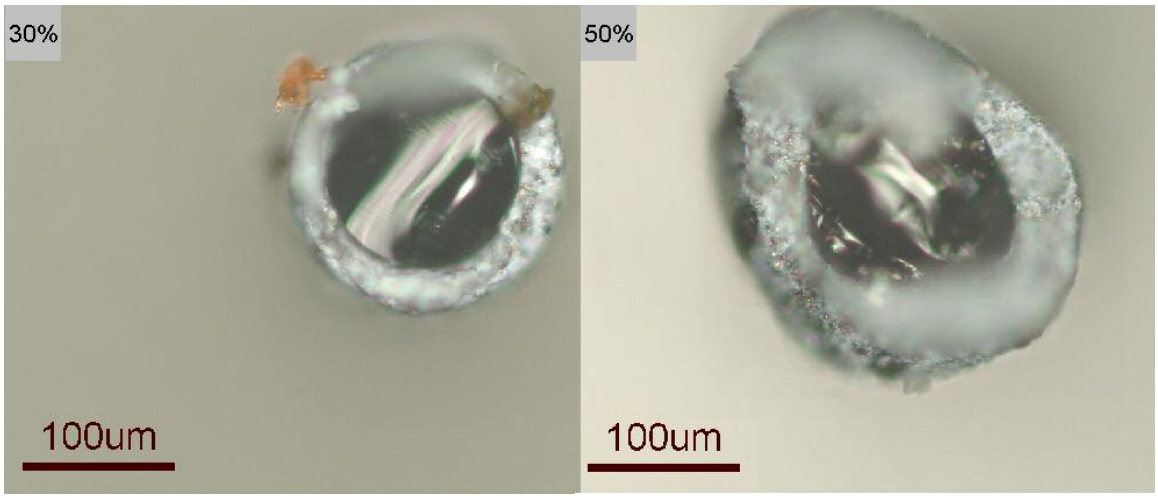

Figure 2.25 Images of cross sectional ferromagnetic paint coated optical fiber taken by an optical microscope.

Measurement done using optical microscope can garner some margin for error, which is within 7 um, because the focal points were fine-tuned to see the surface profile. The static experimental results are plotted in Figure 2.9. Figure 2.26(a) and 2.26(b) show the comparison of the average static displacement on nine repeated data-taking for length 4.2 cm and 5.2 cm with 30% and 50 % nickel by weight.

Displacement D as a function of external magnetic field H based on a quadratic fit can expressed as

$$D(H) = a_1 \cdot H^2 + a_2 H + a_3 \qquad (2.3.46)$$

a_1 , a_2, a_3 are the coefficients for each quadratic fit. Table 2.3 tabulates the coefficients for 4.2 cm and 5.2 cm long optical scanner with different percentage of nickel by mass. In Figure 2.27 a comparison of the 4.2 cm and 5.2 cm-long scanner is given for different percentage of nickel in the coating by mass. These plots are also based on the average values of static displacement for each external magnetic field strength.

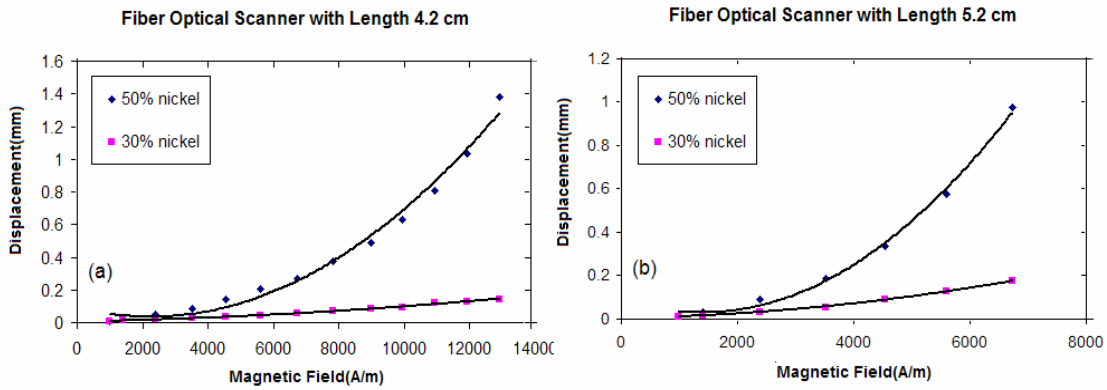

Figure 2.26 A comparison of average static displacement of (a) 4.2 cm and (b) 5.2 cm optical scanner coated with different percentage of nickesl by mass. The static displacement in mm is plotted against the magnitude of external magnetic field strength.

Table 2.3 Coefficients of quadratic fits for the average static displacement measurement based on nine repeated sets of experiments.

% nickel	30%		50%	
Length(c m)	4.2	5.2	4.2	5.2
a_1 H^2	5×10^{-10}	3×10^{-9}	1×10^{-8}	3×10^{-8}
a_2 H	4×10^{-6}	4×10^{-6}	-5×10^{-5}	-9×10^{-5}
a_3 -	0.0045	0.0039	0.0898	0.0913

As expected, the longer the optical fiber scanner, the more the displacement can be achieved. Above 1 mm static displacement can be achieved by 5.2 cm-long optical scanner for both 50% and 30 % of nickel. Since the fiber optical scanners are mechanical

scanners in nature, the repeatability could be an issue for the need of precision control of the displacement. As shown in Figure 2.28, the experiment is repeated nine times for doing an error analysis.

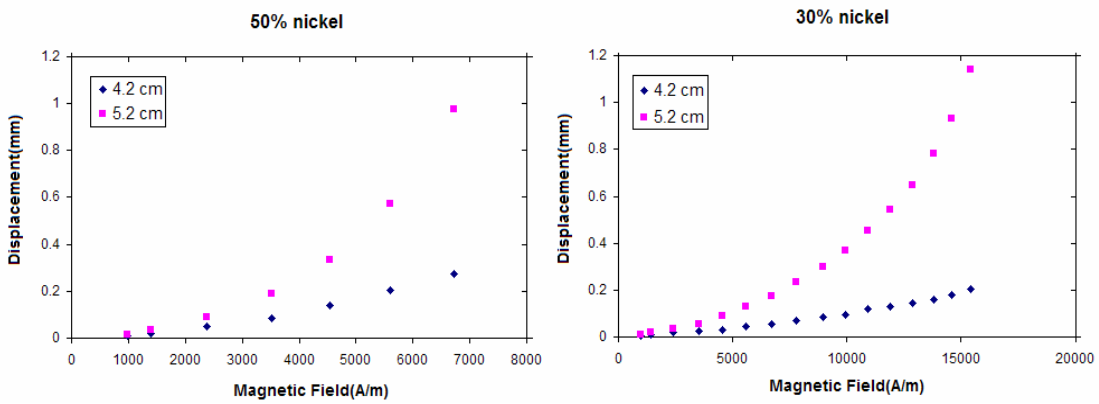

Figure 2.27 For both 50 and 30 percentage nickel coated optical scanner. 4.2 cm and 5.2 cm long optical scanner are compared. The static displacement in mm is plotted against the magnitude of external magnetic field strength.

For 4.2 cm scanner with 50% nickel, displacements fall within 8 % of deviation from the average curve. Similarly, for 5.2 cm scanner with 50% nickel, displacements fall within 3 % of deviation from the average curve. The error bar gets substantially higher as the magnetic field strength is increased up to 9000 A/m. Likewise Figure 2.29 shows the statistical analysis of static measurement for 4.2 cm and 5.2 cm-long optical scanner with 30% nickel. The static displacement falls within 27% and 10% deviation from the average values, respectively. Similarly, the error bar gets large as the magnetic field strength get stronger. Based on the analysis of Figure 2.28 and Figure 2.29 the deviation of static displacement is higher at high input magnetic field. To characterize the scanner device dynamically electric currents are converted to voltage by using a 100K ohm resistors connected in series with the anode and cathode, individually.

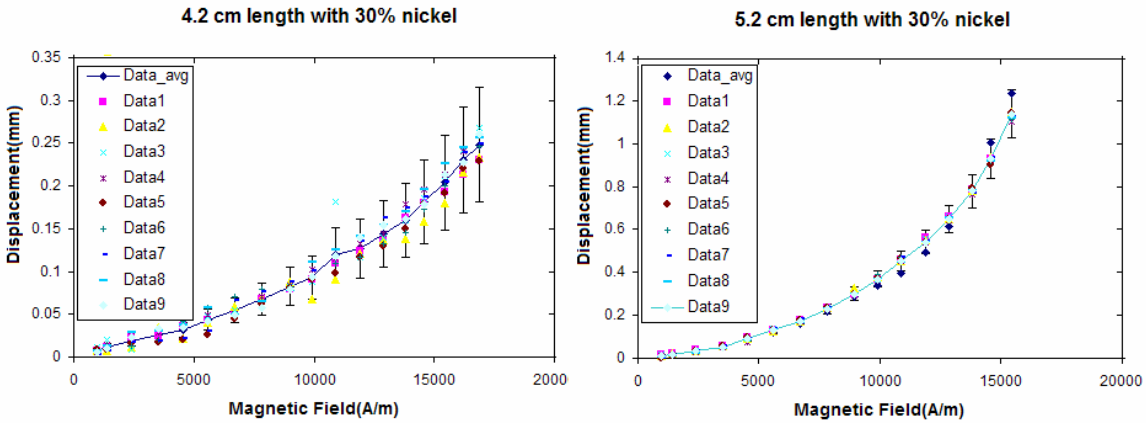

Figure 2.28 Statistical data of 4.2cm and 5.2cm optical scanner with 50% nickel in the coating. The error bar is shown for each data point to indicate the range of margin for error.

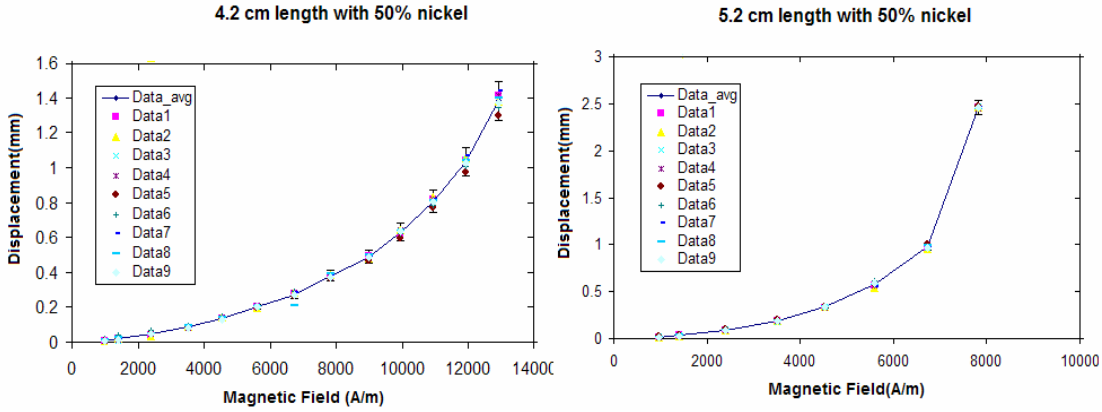

Figure 2.29 Statistical data of 4.2 cm and 5.2 cm optical scanner with 30% nickel in the coating. The error bar is shown for each data point to indicate the range of margin for error.

The dynamic positions of the lsight spot can then be obtained using the electric currents drawn from both electrodes. Figure 2.30(a) and 2.30(b) delineates the amplitude frequency response of a single mode optical fiber and shows the experimental values of fundamental mode resonant frequencies of L_p = 4.2 cm and 5.2 cm with 50% nickel at an input magnetic field amplitude of 5.6 KA/m. The natural frequencies are 31.6Hz and 20.6 Hz under the application of excitation frequencies, which are half of the respective

natural frequencies, and the experimental values suggest 9.6 and 2.4 in percentage difference, correspondingly. The second-mode natural resonant frequencies or the excitation frequencies occur at 31.7 Hz and 20.3 Hz for L_p = 4.2 cm and 5.2 cm, respectively.

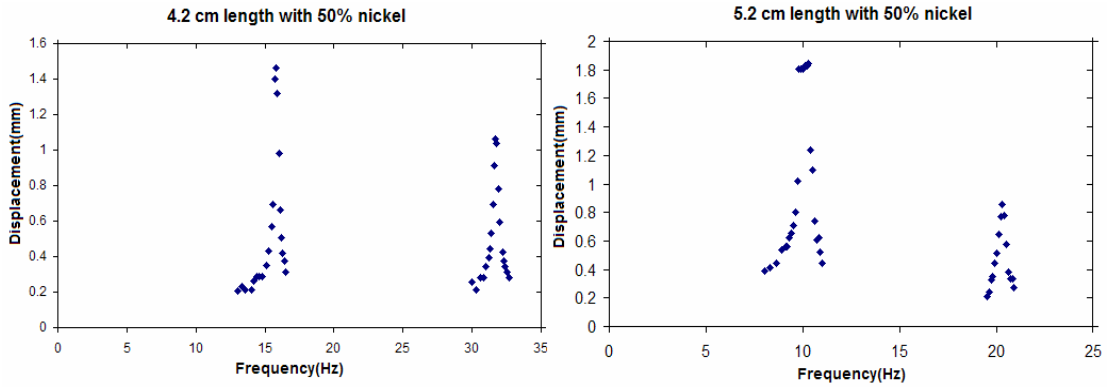

Figure 2.30 Frequency response on displacement amplitude of the optical fiber scanner with 50% nickel in the coating. The results of 4.2 cm and 5.2 cm-long optical scanner are shown. The dynamic displacement is plotted against the frequency of input signal to the electromagnet.

Figure 2.31(a) as well as 2.31(b) show the amplitude frequency response of a single mode optical fiber and shows the experimental values of fundamental mode resonant frequencies of L_p = 4.2 cms and 5.2 cm with 30% nickel at an input magnetic field amplitude of 5.6 KA/m, respectively. The natural frequencies for L_p = 4.2 cm and 5.2 cm are 43 Hz and 26.2 Hz under the application of excitation frequencies, which are half of the respective natural frequencies, and the experimental values suggest 4 and 8.4 in percentage difference, correspondingly. The second-mode natural resonant frequencies, the same as the excitation frequencies, occur at 43 Hz and 26.5 Hz for L_p = 4.2 cm and 5.2 cm, respectively.

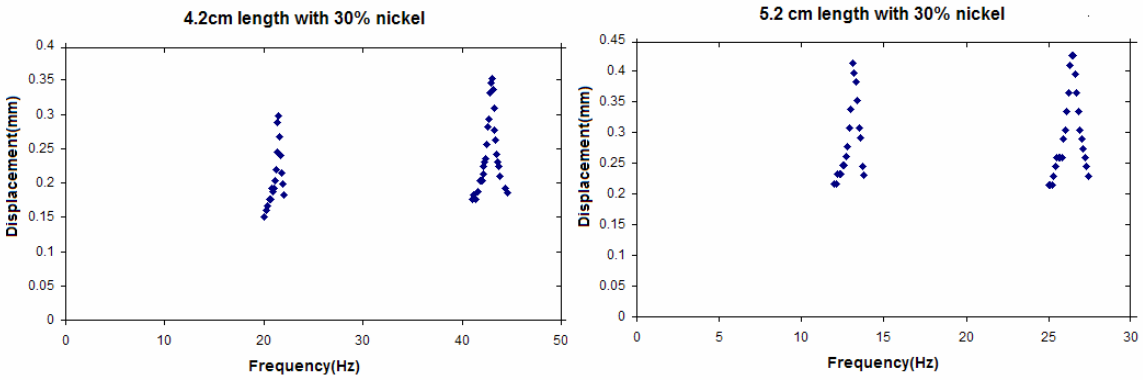

Figure 2.31 Frequency response on displacement amplitude of the optical fiber scanner with 30% nickel in the coating. The results of 4.2 cm and 5.2 cm-long optical scanner are shown. The dynamic displacement is plotted against the frequency of input signal to the electromagnet.

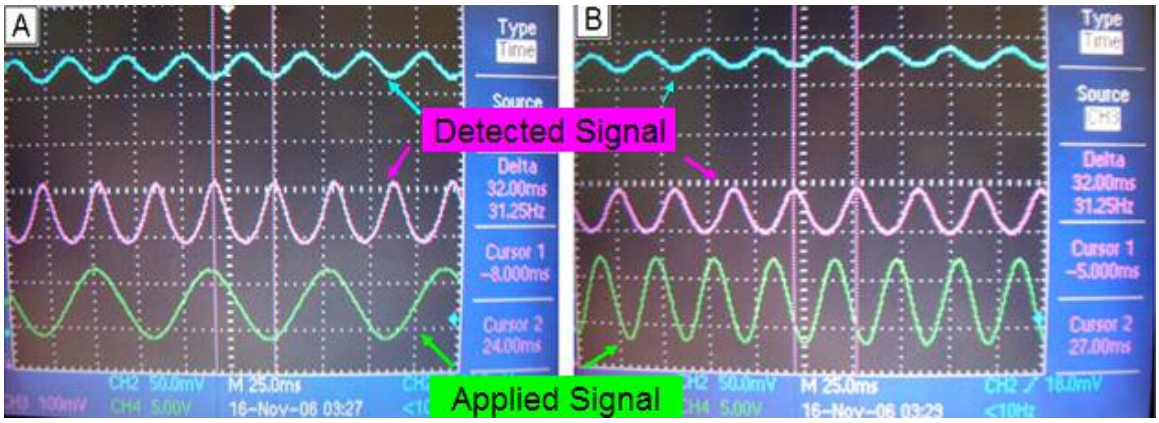

Figure 2.32 The waveforms of applied signal to the electromagnet and detected signals drawn from the position sensing device: (a) 1st mode, (b) 2nd mode resonant frequency.

Upon the comparison between frequency response of figure 2.30 and 2.31 the natural frequencies are different for the scanners with the same length and different percentage of nickel in the coating, and the reason is attributed to the extra mass of 50% nickel coating. Figure 2.32 shows the detected signal waveforms from the position sensing device, and these waveforms are used to determine the dynamic displacement as well as its motion at resonant frequencies.

2.5 Summary and Conclusion

In chapter two, a review of basic magnetic theory. The magnetic theory then leads to the introduction of a variety of magnetic-actuating devices, in which performance and advantages of magnetic devices are summarized for different applications as mentioned from different literature sources. The magnetic device introduction is then narrowed down to fiber optic magnetic devices. Static and dynamic theories of optical fiber devices are then given to support the experimental work. The results of experimental works are then shown to demonstrate the working principle of the fiber optic devices designed at UTA.

CHIAPTER 3

SUITABILITY OF ELECTROMAGNETIC FIBRE OPTICAL SCANNER FOR THE APPLICATION OF OCT SYSTEMS

3.1 Overview

The applications for the fiber optical scanner, as mentioned, are handful. Biomedical imaging is the targeting application and it is particularly suitable because it can be inserted into a limited volume and has no concern for potential damage to the surrounding environment. In the following sub-section optical coherence tomography (OCT) application is discussed and investigated for the use of electromagnetic fiber optic scanner as a sample arm scanning mechanism. First, a review of OCT systems is given to understand the working principle behind it, and also different variance of OCT system is described. And then an analysis of the electromagnetic fiber optic scanner for OCT systems is given and discussed to determine its suitability.

3.2 Brief Introduction to OCT Systems and Imaging probes

OCT is an new imaging modality capable of cross sectional imaging on structure of biological tissues with high axial and lateral resolution. The main merits of OCT imaging lie in its non-invasive, non-contact characteristics with micrometer scale

resolution.[40] The main merits of OCT imaging lie in its non-invasive, non-contact characteristics with micrometer scale resolution.[41] With resolution in micrometer scale OCT system has proven to be a useful diagnostic tool in clinical trials because of its ability to perform precise structural imaging and monitor morphological changes of tissues for the tract of pathology and the detection of diseases.[42-46] Time domain OCT is the most widely implemented system modality; however, fourier domain or spectral OCT has start taken its role as a replacement for its fast speed with stable imaging quality and simplicity in system setup.[47] Different types of OCT system such as polarization sensitive and Doppler OCTs have been developed to enhance contrast and functionality.[48-52] Polarization sensitive OCT has been used to image structure of various biological tissues because natural birefringence of some tissue structures can alter polarization of incident light which adds more detailed structural information to an ordinary OCT image; while Doppler OCT is used to image moving object such as blood cells at the same time taking structural image of surrounding environment. The working principle of OCT systems has been well elaborated in the literatures and is based on low time-coherence in-elastic light scattering or reflection off samples, with which the fringes are formed when interfere with the optical beam of reference path.[53] The optical scanner is to be employed in the sample arm of OCT system in order to provide scanning on a sample. To evaluate the scanner's scanning capability slow scan and fast scan are

performed, and the main issue of non-linearity is addressed. Regardless of types of OCT system been implemented, in order to construct a contour of optical reflectivity map upon a sample 1-D or 2-D scanning mechanism has been an indispensable part of OCT imaging setup. Moreover, a scanning mechanism with small dimensions, easy implementation, and robust functionality has always been desired.

The scanning methods of light delivery for light-object interaction have been an important and on-going research topic in the field of biomedical imaging. Current optical scanning probes are constructed in two ways: directly translate an optical fiber or deflect light beam to provide forward linear scanning and circumferential scanning. MEMS(MicroElectroMechanicalSystem) is a miniaturizing technique that provides devices in small dimensions, low cost, and high versatility in functions. Forward optical scanning probe invented using MEMS technology such as electrostatic, thermal bimorph actuators have been used as a scanning mechanism for in vivo human bladder and eyeball imaging.

3.3 Type of Implemented OCT Systems

In the following sections, implementation of OCT systems are reviewed and shown. The governing principles, system limitation and the respective advantages are discussed and analyzed. The OCT is used to interrogate the performance of the magnetic fiber optic scanner as an OCT probe at slow and high speed scanning.

3.3.1 Time-Domain OCT

In OCT systems, requirement of the speed of the sample arm scanning is governed by the nature of the OCT system being implemented. For instance, the sample scanning speed in time-domain OCT(TD-OCT) is limited by the speed of time delay mechanism in the reference arm due to the nature of sequential scanning of the system.

To evaluate the slow-scan capability, a primitive TD-OCT is setup and lay out as shown in Figure 3.1(a) and (b). As shown in the figure part (a), a near-infrared broadband light source at wavelength of 1550 nm (JDS Uniphase Technolgies) with 3 mW of optical power is coupled into a 2 x 2 optical coupler(Thorlabs Inc. USA). Equal amount of power is divided into two paths, namely, the reference and sample arms. The beam to the reference arm is collimated by a collimator and shone onto a piece of silicon wafer coated with gold.

The beam to the sample arm is directly guided by an optical fiber, focused by a GRIN lens(Newport Corporation, USA), and shone onto a sample. The focal spot size is about 34 um, and the working distance is about 2.5mm. A 3 mm by 3 mm gold-coated silicon wafer is mounted on a speaker, which is served as reference scanner, and the purpose of a reference scanning device is for scanning into the depth direction of a sample. The amount of power coupled into sample arm is about 1mW. The scan speed of the speaker is limited at 100 Hz to optimize its scan range into the sample.

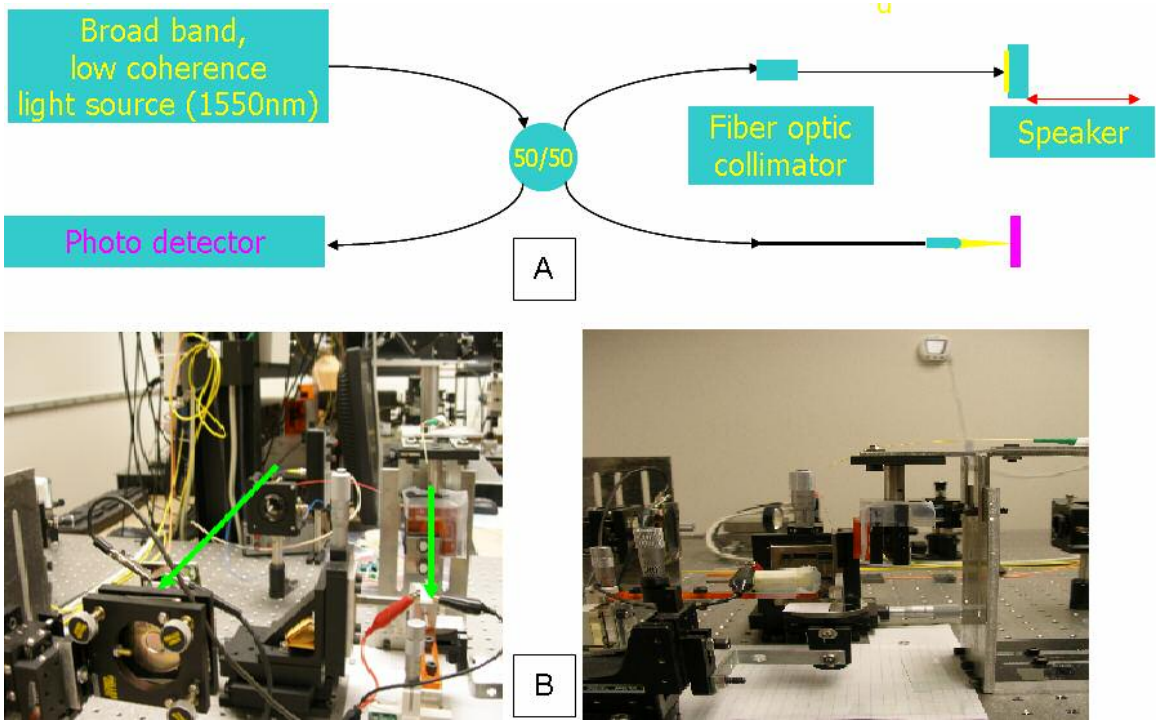

Figure 3.1 part (a), a Time-Domain OCT experimental layout diagram. Part (b), a real experimental setup on an optical bench: a whole view from the side and a side view.

A compromise has to be made between the scan range and the scanning speed because a larger scan range implies a broader range of velocity experiences by the gold-coated silicon wafer. A broader range of velocity means broader frequency bandwidth of fringes due to Doppler effect. Therefore, the Nyquist frequency relationship has to be satisfied between the maximum data acquisition rate and the maximum fringe frequency, otherwise, a complete fringe signal cannot be acquired or loss the signal information can happen. And this requirement also limits the axial resolution from system's point of view. Figure 3.2 is an experimental data, in which fringe frequency is plotted against input voltage. The consequence of the figure is that the fringe frequency increases as the voltage input to the speaker increases.

And figure 3.1 part (b) shows the actual experimental setup. The sample arm and reference arm are marked by green lines, and also, the side view shows the sample arm going vertically. In the detecting end, the detected optical beam is coupled into a photdetector for signal acquisition.

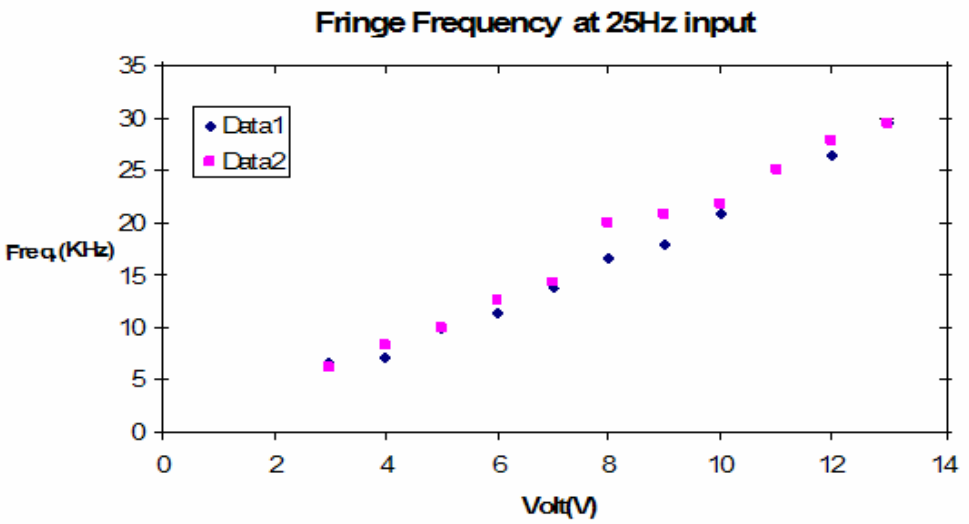

Figure 3.2 Experimental plot of fringe frequency as a function of voltage amplitude input to a speaker.

3.3.2 Spectral-Domain OCT

Spectral-Domain OCT, as already told in its name, retains the signal information in the spectrum of the infrared light beam. Comparing with the Time-domaisn OCT, spectral domain OCT has advantages in several fronts. In SD-OCT, the depth information is encoded in the spectrum of the light beam; therefore, unlike the need of reference scanning for a full focal-depth interrogation, SD-OCT provides the reflectivity information in a full focal depth at the same time, and it is capable of better efficiency in scanning. Also constrains of the reference scanning such as slow speed, nonlinearity in scanning in TD-OCT is evaded using SD-OCT; therefore, SD-OCT provides much more frames of images for a second and a more stable imaging quality.

3.3.3 Experimental Setup for Spectral-Domain OCT System

In figure 3.3, a layout of a spectral-domain OCT diagram is shown. An infrared broadband Ti-Sapphire laser (Kapteyn – Murnane Laboratories, Boulder, CO) with a full width at half maximum bandwidth of 45 nm center at 780 nm is coupled into an 2 x 2 optical coupler(Thorlabs Inc. USA). Equal amount of power is directed into sample and reference paths. In the reference, the optical beam is collimated and shown onto a mirror, which is fixed at a location for interferometric matching in optical path length. In the sample path setup, it is the same as implemented for TD-OCT. At the detecting end, the spectrum of light beam is analyzed by a spectrometer. The light beam is coupled by a collimator. The wavelength components are spread by an optical grating, and a lens redirects all wavelength components for CCD camera detection (Hamamatsu corporation, Japan), which reads the spectrum of the light beam.

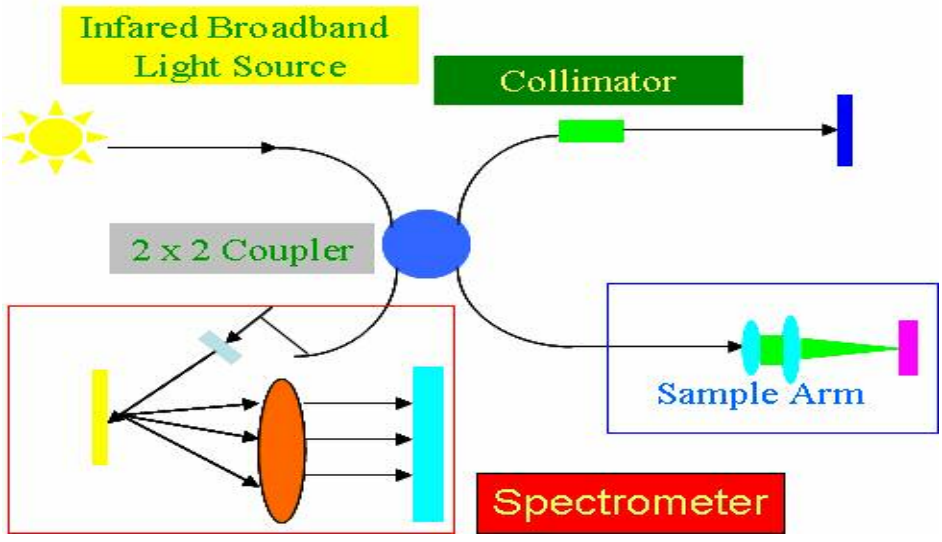

Figure 3.3 A layout diagram of spectral-domain OCT.

By applying fast fourier transformation(FFT) and signal processing on the acquired signals, interference fringes can be extracted.

3.4 Performance of the Fiber Optical Scanner as an OCT Probe

In this section, results of cross-sectional images using TD-OCT and SD-OCT are discussed. The scan waveform and quality of images allow the evaluation of performance of electromagnetic OCT probe. Linearity in terms displacement as a function of time as well as the degree of orthogonal deviation to a single-line scan. In TD-OCT, since the speed of reference scanning speaker is limited at 100 Hz. In order to optimize the image resolution number of depth scan or reference scan for a single line scan has to be maximized. Consequently, the speed of electromagnetic fiber optic scanner has to be as low as possible and is set to be 250 mHz.

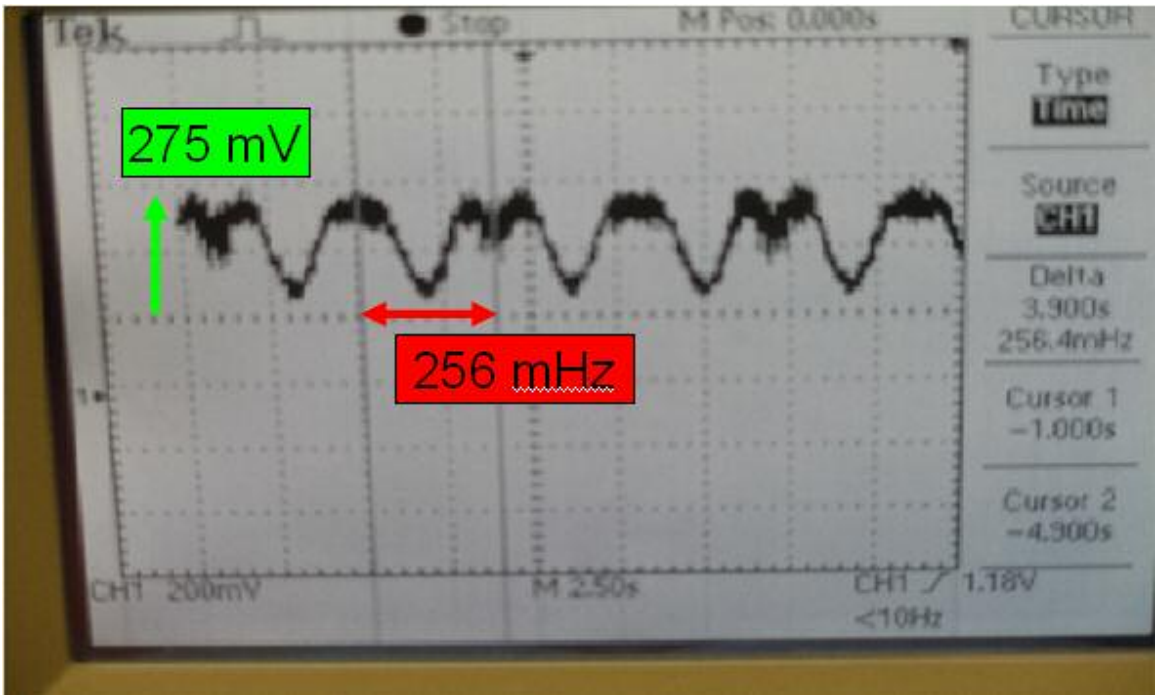

Figure 3.4 Scanning waveform of the electromagnetic fiber optic scanner at 250 mHz with input voltage of 10 V.

Probe scanning at 250 mHz corresponds to four seconds for completing one entire scan. Reference scanning at 100 Hz implies 200 depth scans in one second, and the reference scanning speed ultimately limits the transverse resolution from system's point of view. Also the light beam focused by GRIN lens has beam spot of about 34 um, which determines the transverse resolution from optics point of view. Figure 3.4 show the scanning waveform for the electromagnetic fiber optic scanner, which has the modulation efficiency of 85%. In an ideal case, the light delivers to the sample should be constant along the scan range for optimizing the signals fed back. Figure 3.5 shows the cross-sectional image of red onion by the TD-OCT setup shown in the previous section.

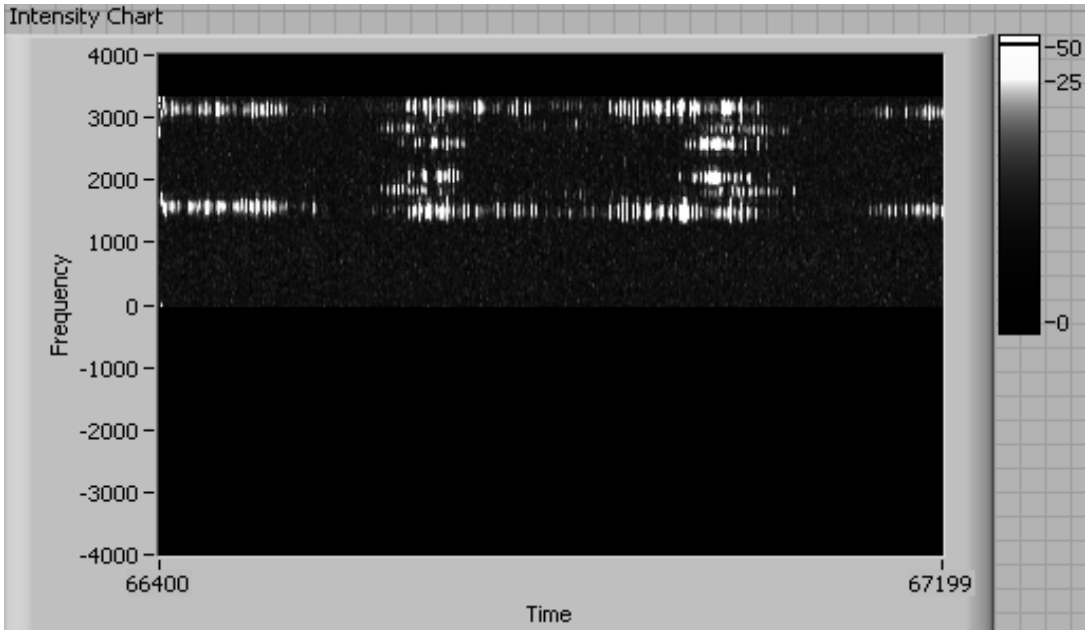

Figure 3.5 Cross-sectional image of red onion using TD-OCT setup described above.

The surface and cells of red onion can be seen from this image, and it suggests that the electromagnet fiber optic scanner is capable of slow scan. However, since the speed of

reference scanning speaker is limited at 100 Hz, and wide range of velocities give wide range of doppler shifted fringe frequencies the axial and transverse resolutions are limited. Also the optical dispersions due to mismatches in materials and polarization between sample and reference arms reduce the resolution since the signals are broadened due the effect.

Video rate scanning has more value in the clinical applications since it updates images in a faster rate. In the following, electromagnetic fiber optic scanner is tested using Spectral-Domain OCT for its fast scan capability. Figure 3.6(a) shows the scan-

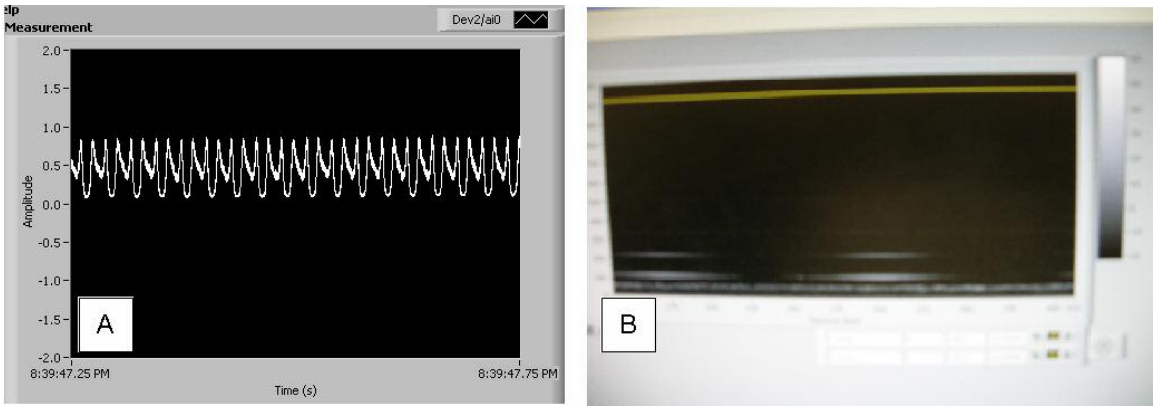

Figure 3.6 (a) The scanning waveform at the resonant frequency of 66 Hz of the electromagnetic fiber optic scanner. (b) Image taken on a glass slide on top of paper.

waveform at the resonant frequency. The modulation efficiency of the scan is well over 100%, which is undesirable for doing imaging. In addition the linearity of the scan is poor, which reflects the result of images at the fast scan using electromagnetic fiber optic scanner as shown in Figure 3.6(b). There are some possible causes for nonlinearities of the image shown in figure 3.6(b). First, the magnetic field induces force on the optic fiber can move the optical fiber in many different directions since the gradient of

magnetic field varies along the scan range. In addition the magnetic field generated by the electromagnet is unknown and might be dedicated for other applications. The field pattern might be undesirable for generating a linear scan. Second, since the optical fiber is circular in its geometry it can easily subject to any forces acting upon it.

3.5 Summary and Conclusion

In this chapter, a brief introduction is given to illustrate the existing scanning device for OCT systems. Experimental setups for Time-Domain OCT and Fourier-Domain OCT are shown and explained in detailed. Time-Domain OCT encountered difficulties during the course of experiment such as non-linearity and scan speed of scanning device in the reference arm. On the other hand, fourier-domain OCT provides compactness in system setup; thus, it provides faster imaging speed and more stable imaging quality. However, it was determined that the oscillating optical fiber gives rise to huge line-scan non-linearity; therefore, poor imaging quality is presented.

CHAPTER 4

AN ALTERNATIVE WAY OF IMPLEMENTING ELECTROMAGNETIC ACTUATION

4.1 Overview

The original idea is to build an optical scanner by taking advantages of the size of an optic fiber. The analysis of the electromagnetic fiber optic actuator in the previous sub-sections explains why the fiber optic actuator might not be suitable for the imaging application: unknown magnetic field pattern makes it difficult to position the fiber optic actuator for a scan with better linearity, external forces can easily influence the fiber optic actuator due to its physical geometry and dimensions. Since magnetic field plotter and design parameters electromagnet are not available the solution to the nonlinearity problems has to come from the actuator itself.

4.2 Solutions to the Electromagnetic Actuator as an OCT probe

The solution implemented to the nonlinearity is to swing a rectangular cantilever instead of an optical fiber. With 0.5 mm thick ferromagnetic-paint coated on a card board substrate, which is attached on a PVC plastic cantilever at 5 mm away from the tip of the cantilever, an optical assembly mounted on the cantilever can then be steered using external magnetic field source. Different dimensions and different materials of a rectangular cantilever can be used to tailor specific performance requirement. The first

generation device is 3.19 mm by 0.64 mm by 4 mm in width, thickness, and length, respectively.

The area moment of inertia I for the given dimensions and material is 2.78746 $\cdot 10^{-13}\ m^3$. The calculated natural resonant frequency is 86.69 Hz. The empirical value of the natural resonant frequency is 75.6 Hz, which has 12 % difference from the calculated value.

Figure 4.1 shows the optical assembly of magnetic scanning probe. A glass optical- fiber ferrule is used to mount and fix the position of an 8^o angle-cleaved optical fiber, which is kept 0.4 mm away from a GRIN lens (Newport Corporation, USA), which gives image distance of 3.8 mm away. The optical fiber is angle-cleaved to evade back- reflection due to refractive index mismatch of mediums. The whole optical assembly is fixed using epoxy glue.

The theoretical calculation of focal spot size, which signifies the transversal resolution of the scanning probe, is 18 μm for the set distance between GRIN lens and the tip of the optical fiber, and the corresponding confocal parameter is 0.613 mm for the calculated spot size.

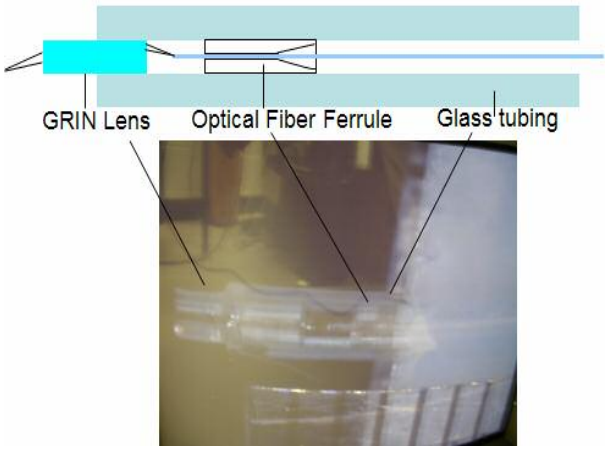

Figure 4.1. A diagram and a picture of optical assembly of magnetically actuated probe are shown. A glass ferrule holds an angle-cleaved optical fiber. With light shunt on a GRIN lens, which focuses the light beam. Also a millimeter ruler is used to show the dimensions of the assembly.

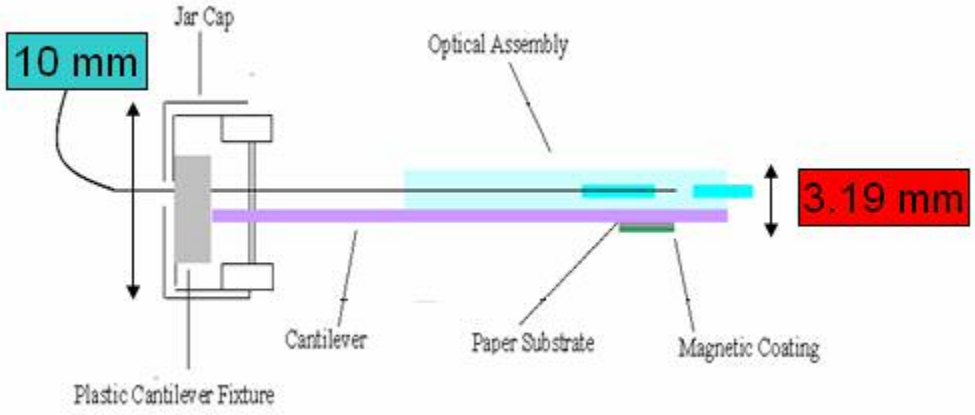

Figure 4.2. Structure of magnetic probe assembly composes of an optical assembly, magnetic coating, and 4 cm cantilever. The optical assembly and magnetic coating are mounted on the cantilever, which is attached to an acrylic plastic fixture. The fixture is glued with a jar cap.

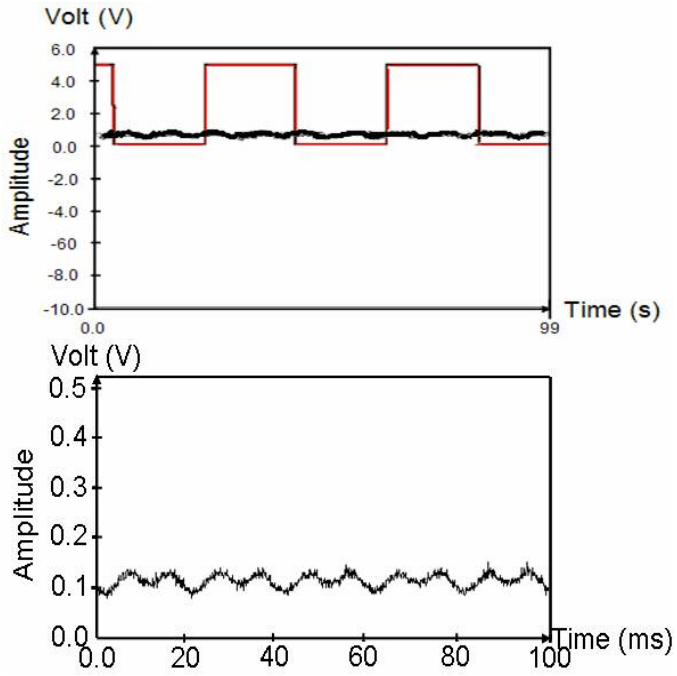

Figure 4.3 Scanning waveforms of the magnetic probe on a mirror. The top figure depicts the rectangular triggering signal in comparison with the scanning waveform of the magnetic probe. The bottom figure is a zoom-in of the scanning waveform.

Figure 4.2 is composed of an optical assembly on one side of a cantilever with magnetic substrate on the other side. The device dimensions are 3.19 mm by 0.64 mm by 4 mm in width, thickness, and length, respectively. As shown in Figure 4.2 the plastic cantilever is attached on a plastic fixture, which is glued with a cap of a plastic bottle. The scanning waveform of the magnetic probe is depicted in Figure 4.3, which shows the repeatability and the linearity of scans, has an optical modulation efficiency of 41%. Figure 4.3 also shows the scanning rate of the scanner to be twice as fast as the triggering signal for data acquisition since the natural frequency of the scanner is twice as fast as the excitation frequency. The performance of the scanner is capable of 0.5 mm of scan range.

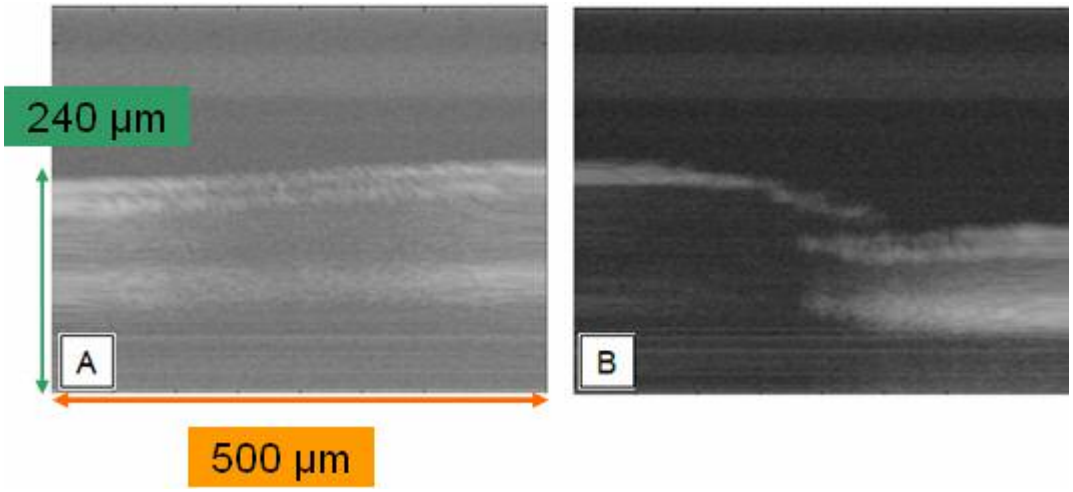

Figure 4.4 The in vivo images of (a) finger nail, (b) finger cuticle.

4.3 Characterization of the Extended Electromagnetic Rectangular Actuator

The proposed electromagnetically actuated rectangular cantilever was shown. It is demonstrated for its capability as an OCT imaging probe. The scanning range is limited at 0.5 mm with input voltage of 9V. As mentioned in the previous sections, attractive magnetic force is induced due to interaction of ferromagnetic powders and external magnetic flux. In order to increase the scanning range there are several possible strategies available: The increase of additional input voltage, cantilever dimensions, and materials of cantilever. However, additional input voltage might not be desirable because large scanning range at high speed could cause unnecessary damping, which is detrimental to imaging quality, and that still need to be proved experimentally. PVC cantilever is cut from a PVC sheet, which is used because it is cheap and readily available. In the following sections the increase in scanning range is demonstrated by changing the cantilever dimension and structure.

4.3.1 Extended Probe Implementation and Optical Characterization

Though, a scanning distance of 500 μm is demonstrated using a cantilever based actuator, it is not practical for clinical applications. Thus, an improve scanner with a scan distance about or greater than 1 mm is desirable. Figure 4.5 shows the improved electromagnetic probe. The device dimensions are 3.4 mm by 0.64 mm by 7 mm in width, thickness, and length, respectively. It is very similar the one shown in Figure 4.2 with an exception that the optical assembly is mounted on an extended bar, which is attached to the original 4cm cantilever. Experimental setup is in figure 4.6.

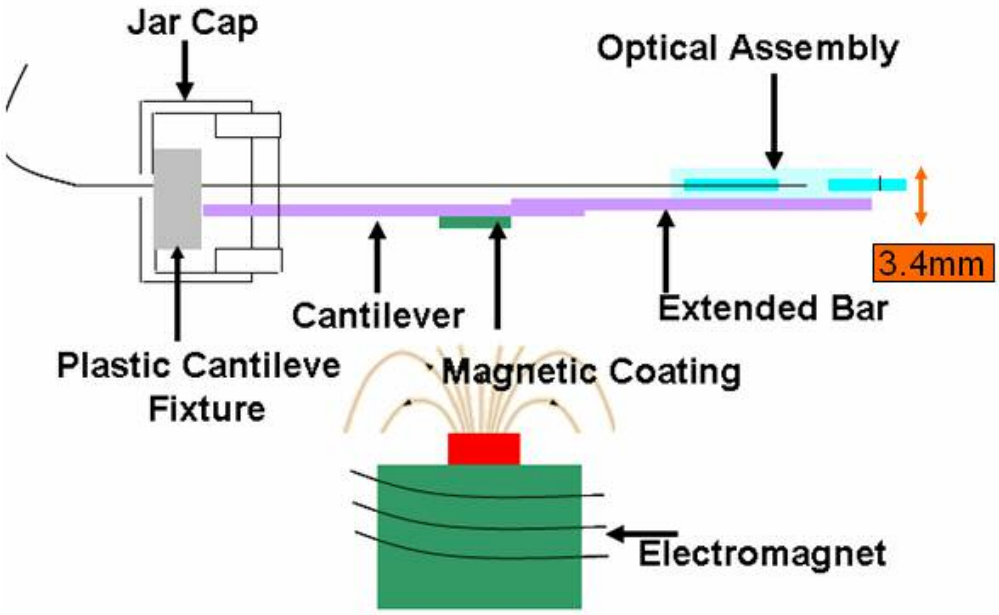

Figure 4.5 Structure of magnetic probe assembly composes of an optical assembly, magnetic coating, and cantilever. The optical assembly and magnetic coating are mounted on the cantilever, which is attached to an acrylic plastic fixture. The fixture is glued with a jar cap. An electromagnet is kept ~0.5mm away.

The light coupled into sample arm is directly guided by an optical fiber and focused by the in vivo imaging probe, which is mounted on a fixture-stand as shown in the figure. An electromagnet is about 0.5 mm away from the magnetic coating. As shown and

mentioned in the previous sections, a line-scan linearity in terms of optical power being fed back is critical in a tomographic generation because maximal optical signals scattering or reflecting from the sample is desirable. Herein, the scanning waveforms at 20 Hz with input 12V, and 15V are shown in Figure 4.7(a) and (b), which shows the repeatability and the linearity of scans, has an optical modulation efficiency of 66% and 95%, respectively. Figure 4.7 also shows the scanning rate of the scanner to be twice as fast as the triggering signal for data acquisition since the natural frequency of the scanner is twice as fast as the excitation frequency.

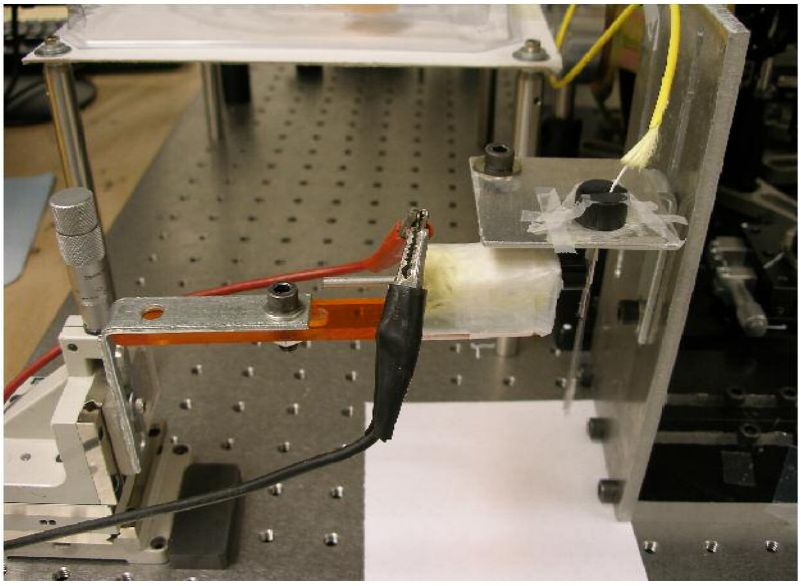

Figure 4.6 Experimental setup for In Vivo cross-sectional imaging probe.

The maximum power being fed to sample is 2 mW with FWHM spectral bandwidth of 49 nm, which is shown on Figure 4.8. The bandwidth of input light source is important because it directly translate in the depth resolution. The magnetic probe is used to perform in vivo imaging on fingers. Figure 4.10 shows the characterization of dynamic

scanning distance at the resonant frequency of 20 Hz. As depicted by Figure 4.10, the scanning distance increases as the input voltage gets higher.

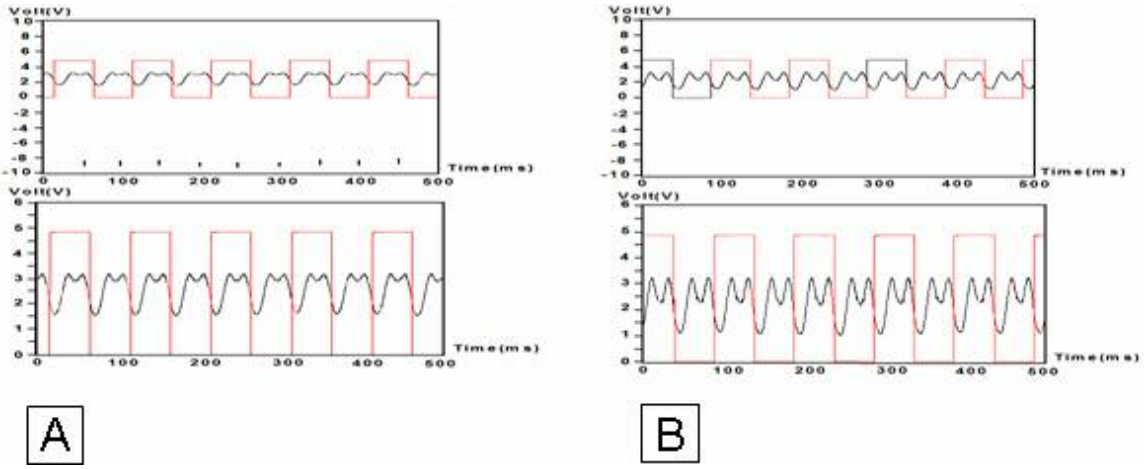

Figure 4.7 (a) is the result for voltage input of 12V, part (b) for voltage input of 15V. Scanning waveforms of the magnetic probe on a mirror. The top figure depicts the rectangular triggering signal in comparison with the scanning waveform of the magnetic probe. The bottom figure is a zoom-in of the scanning waveform.

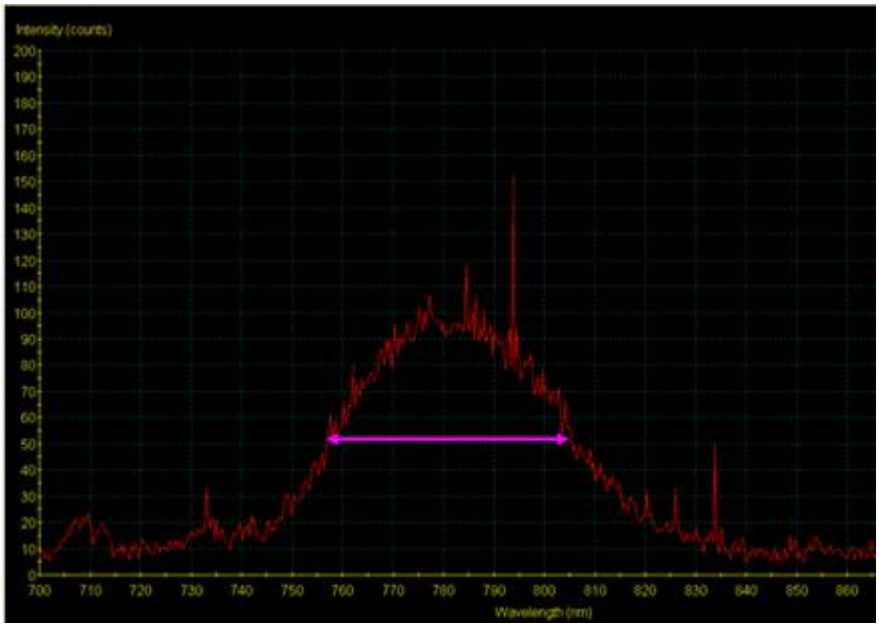

Figure 4.8 Spectral bandwidth of input infrared light. The FWHM spectral bandwidth is about 49 nm.

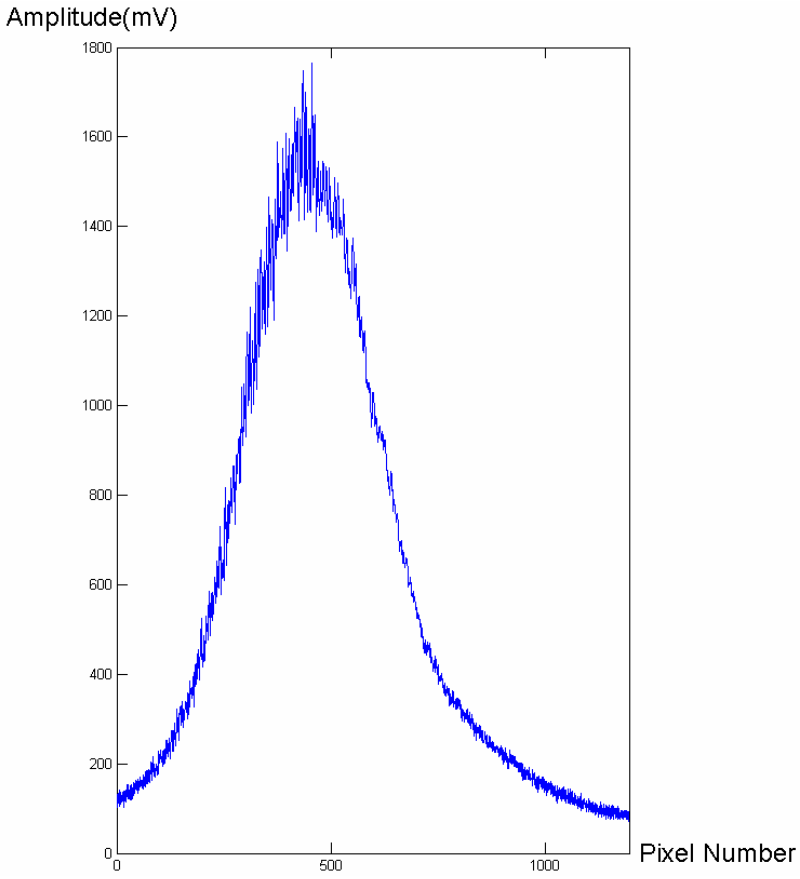

Figure 4.9 Example of interference fringe as a result of in vivo cross-sectional imaging.

However, larger scanning distance is not achieved without cost. Figure 4.11 is a plot of modulation efficiency as a function of input voltage. As shown, the modulation efficiency, which concerns the repeatability and linearity, gets worse as the input voltage rises. An example of interference fringe signal is shown in figure 4.9. The entire bandwidth contains information for one entire depth scan; in another words, different wavelength corresponds to different depth within samples. By stacking depth scans, an imaging reconstruction can be done.

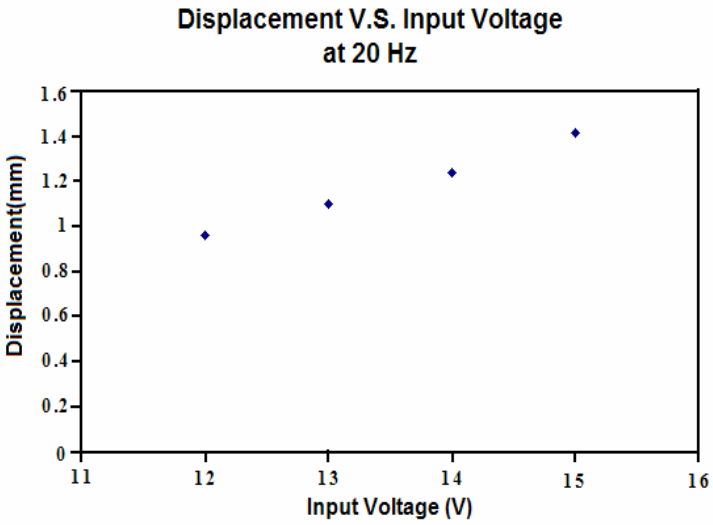

Figure 4.10 Dynamic displacement as a function of input voltage at natural resonant frequency of 20 Hz.

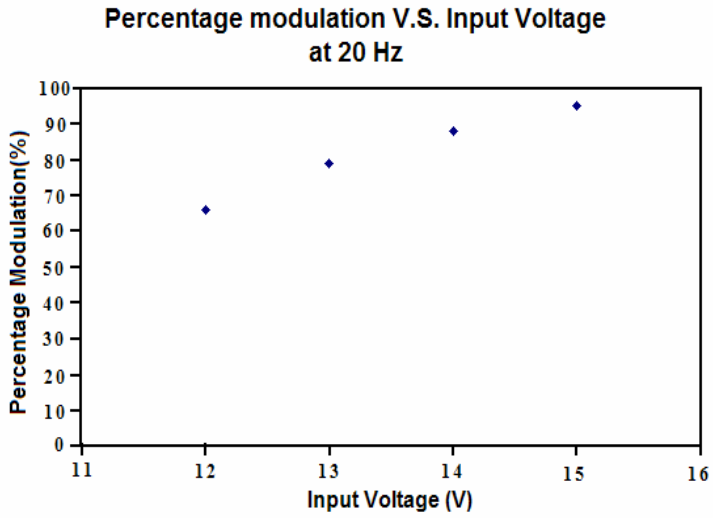

Figure 4.11 Modulation efficiency as a function of input voltage at natural resonant frequency of 20 Hz.

4.3.2 In Vivo Imaging

The extended electromagnetic OCT probe is constructed to meet the requirement of the scanning distance greater than 1 mm. In vivo imaging on fingers is performed to interrogate the probe's performance as an OCT scanning tool, and SD-OCT is the workhorse for carrying out imaging. For the following experiment for extracting the cross-sectional images, a Titanium-Sapphire source, which outputs an infrared broadband laser beam centered at 780 nm with power of 340 mW and bandwidth of 49 nm at half of full wave maximum is used. The bandwidth of the infrared laser allows axial resolution of 5.46 um. Since the same optical assembly is used, the transversal resolution of the scanning probe remains at 18 μm. Similar as previous experiments, since the ferromagnetic paint coated optical scanner is connected to the optical fiber coupler through a FC/APC adaptor, optical cement is used to reduce insertion loss from air to optical fiber and visa versa. The maximum power being fed to sample is about 2 mW. With index finger placed at the working distance of imaging probe, in vivo imaging scanning is perform at input voltage 12 V and 15 V, and different parts of finger nail is performed. Figure 4.12 shows the in vivo images on fingers using a voltage input at 12 V. In part (a) of Figure 4.12 shows in vivo imaging on the cuticle of a finger. Part (b) and (c) of Figure 4.12 shows the in vivo imaging on the finger nail and its underneath structure. Part (d) shows the in vivo imaging of the back-finger and its underneath structure. Similarly Figure 4.13 shows the in vivo images on fingers using a voltage input at 15 V, which gives more scanning range and less light coupling between sample and focal volume of the light beam.

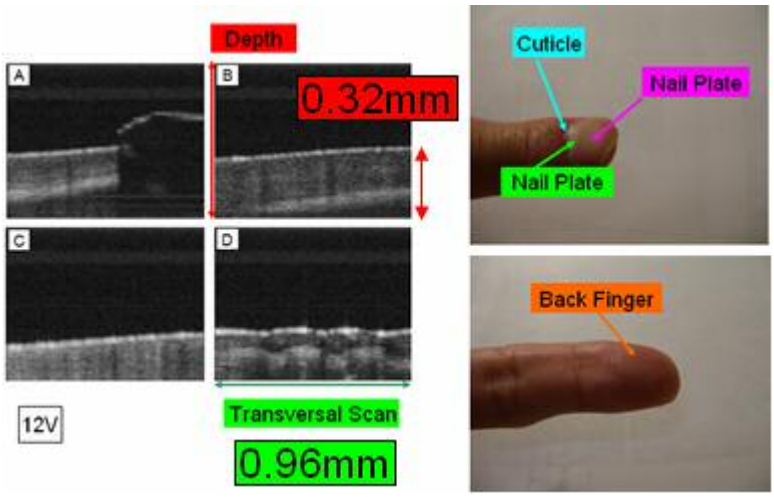

Figure 4.12 Images with the input voltage of 12 V. 4.9(a) is the cuticle portion of an index finger, 4.9(b) and 4.9(c) are in vivo images of finger nail, 4.9(d) is an back-finger image.

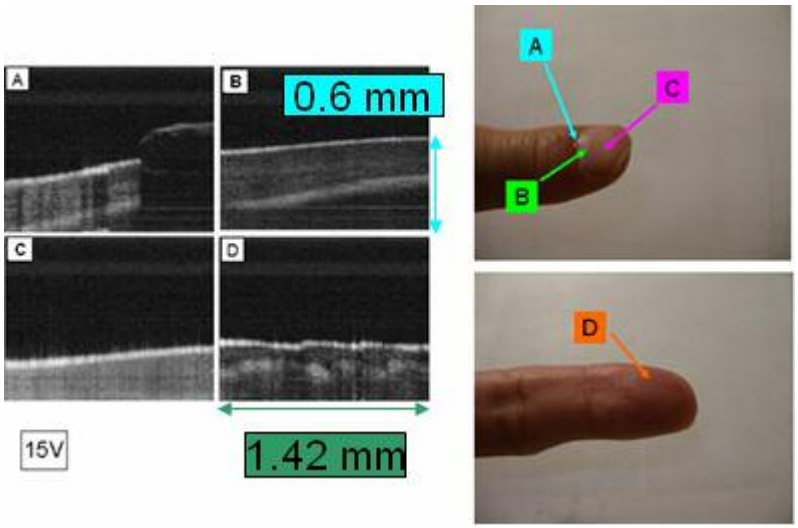

Figure 4.13 Images with the input voltage of 15 V. 4.10(a) is the cuticle portion of an index finger, 4.10(b) and 4.10(c) are in vivo images of finger nail, 4.10(d) is an back-finger image.

4.4 Summary and Conclusion

In this chapter, an alternative solution of magnetic actuation for OCT imaging system is proposed, implemented, and demonstrated with in vivo imaging on finger. The proposed solution is based on a PVC rectangular cantilever with an optical assembly

mounted on top and a magnetic coating attached on the bottom. 500 μm scan range is achieved with cantilever with 4 cm in length. To increase the scan length up to 1 mm, an extra extension of rectangular plate is attached to the original cantilever, and the overall length is then 7 cm. With input voltages of 12V and 15V, in vivo cross-sectional images of index finger are obtained and the imaging sites are also indicated. A scan length of 1.42mm and maximum depth of 0.6mm are achieved with 15V as an input voltage.

CHAPTER 5

CONCLUSION

In this dissertation, the main theme is to demonstrate the feasibility of magnetic actuation in OCT scanning application. Two schemes of magnetic actuation is proposed and interrogated as potential fast-scanning mechanisms for an OCT system: an optical fiber as an actuator and a rectangular cantilever as an actuator. For the actuator based on an optical fiber, static and dynamic experiments were performed to characterize its displacement capability. In static experiments, displacement of 4.2cm and 5.2cm optical fiber with 30% and 50% nickel by weight in the coatings are characterized as a function of D.C. magnetic field. For 4.2 cm optical fiber, the largest displacements are 0.05 mm and 0.35 mm for 30% and 50% nickel coating at magnetic field strength of 7000 A/m, respectively. For 5.2 cm optical fiber, the largest displacements are 0.1 mm and 1 mm for 30% and 50% nickel coating at magnetic field strength of 7000 A/m, respectively. Also, the result of statistical data shows that the deviation of static displacement is progressively larger as the magnetic field strength gets higher. Dynamic testing, a main focus of this dissertation, depicts the displacement amplitude frequency response. Displacement amplitude frequency response delineates the dynamic displacement as a

function of external excitation frequency and the natural resonant frequencies. At 100 mA of input current amplitude 1mm displacement can be achieved for 50% nickel coating, and likewise, between 0.3 mm to 0.4 mm is achieved for 30% nickel. Also, since 50% nickel coated optical fiber carry more mass, its resonant frequency is higher than that of 30% nickel coated optical fiber under the condition of same length. The dynamic testing also elucidates the scanning displacement as a function of time to be sinusoid.

OCT imaging system is our targeting application. In the second part of this work, the suitability of fiber optic scanner is interrogated. Linearity and stability are the main issues in performing OCT imaging. As mentioned in the previous chapters, the induction of magnetic force is due the interaction between magnetic field gradient and magnetic medium. Since magnetic field gradient varies drastically from one point to another the force subjected on the fiber optical scanner differs tremendously in magnitude as well as direction. Moreover, the geometry of an optical fiber is circular and has the same resonant frequency in. Therefore, it is concluded that electromagnetic actuated optical fiber is not suitable for OCT application.

An alternative solution based on magnetic actuation is proposed and demonstrated for its potential in OCT application. A cantilever cut off from a PVC sheet is used as the basic structure for the OCT probe. A paper substrate with magnetic coating is glued to one side of the cantilever, and an optical assembly is mounted on the other side of the cantilever. 500 μm of scan distance is achieved. To add more scanning distance, an extra length of tubing is attached to the cantilever. For input voltages from 12 V to 15 V, the

scanning displacement from .96 mm to 1.42 mm is capable. In vivo images on fingers are obtained using these OCT probes as shown.

Table 5.1 A summary of actuators built for OCT imaging system.

Actuation scheme	Probe Dimensions(mm)	Imaging speed/ input	Scan Type	Authors
Electrostatic (Capactive)	3mm wide 1cm long	4-8 Frames / s 65V	140°	Zara GWU [54]
Micromotor (electromag.)	1.9mm diameter	1 Hz 1V	360°	Chen UC, Irvine [39]
Electroactive Polymer	30 mm X 2 mm 0.3 mm thick	1Hz 2V	Forward scan 3 mm	Chen UC, Irvine [56]
Thermal bimorph	1mm X 1mm cm scale	5 frames / s	37°	Xie CMU [57]
Piezo-electric	2.68mm diameter	8 frames / s	Forward scan 2mm	Fujimoto MIT [14]
Magnetic	3.19mm*2.6mm 7 mm in length	40 frames / s	Forward scan >2mm possible	UTA

Table 5.1 shows a summary of actuating devices built for OCT imaging probes. Besides the magnetic device developed here at UTA, the rest of devices are implemented in a Time-domain OCT(TD-OCT). Because of the nature of the imaging modality, the scanning speed is rather limited as mentioned in chapter 3, other device speed can be much higher. For example, piezo-electric scanning done by Fujimoto et. al. claimed that device speed of 100 Hz is possible. Devices with a variety of scan types are implement with different optics implementation or nature of actuation scheme. For example, micromotor generates rotary motion, which can be used for circumferential imaging. A prism can redirect optical light and perform side scanning.

Though magnetic actuation can provide large magnetic force, it has some drawback for in vivo imaging application. The magnetic force drops exponentially with distance away from the magnetic coating. This could pose a potential problem when

perform scanning inside human body, and different magnetic field source and higher magnetic field strength might be needed. Also, the interaction of magnetic field and biological tissues might be a hindrance to magnetic actuation, and the interaction is yet to be determined. Moreover, the current device dimension with 7 cm in length is not practical for clinical used since organs have limited volume to perform imaging. In the future several works need to be addressed: simulation of magnetic actuation in biological environment; and magnetic devices with requirement of smaller magnetic field strength in the range of few hundred A/m is needed for the endoscopic testing.

REFERENCES

1. Hiram C. Polk, Jr. Bernard Gardner, H. Harlan Stone, Basic Surgery 5th edition, St. Louis Missouri, Quality Medical Publishing.
2. P.R. Salmon, Fiber-Optic Endoscopy, Grune & Stratton, Inc. Ch1.
3. Raymond K. Kostuk and James Carrier, "Interconnect Signal Channel Density of Fiber Imaging Guides," Parallel Interconnects, 1999 (PI'99) Proceedings, The 6th International Conference, 1999 pp.157-164.
4. Etsuko Kobayshi, Ken Masamune, Ichiro Sakuma, and Takeyoshi Dohi, "A Wide-Angle View Endoscope System Using Wedge Prisms," Surgical Endoscopy, Vol. 18, No. 9, pp. 1396-1398, September 2004.
5. Alessandra Pedrocchi, Storrs Hoen, Giancarlo Fergno, and Antonio Pedotti, "Perspectives on MEMS in Bioengineering: A Novel Capacitive Position Microsensor," IEEE Transactions on Biomedical Engineering, Vol. 47, No. 1, January 2000.
6. L.M. Gao, Y. Chen, L.M. Lin, G.Z. Yan, "Micro Motor Based A New Type of Endoscope," Proceedings of the 20th Annual International Conference of the IEEE Engineering in Medicine and Biology Society, Vol. 20, No. 4, 1998.
7. Koji Ikuta, Makoto Nokata, "Two-lead-wire Drive for Multi-Micro Actuators," Proceedings of the 1999 IEEE International Conference on Robotics & Automation Detroit, Michigan, May 1999.
8. De Dobbelaere, P.; Falta, K.; Gloeckner, S.; Paltra, S. "Digital MEMS for Optical Switching," IEEE Communicatios Magazine, Vol. 40, No. 3, pp. 88-95, March 2002.
9. Eugene Hecht, OPTICS, Third Edition Addison-Wesley 1998, pp. 400.
10. Michael R. Hee, Joseph A. Izatt, Eric A. Swanson, David Huang, Joel S. Schuman, Charles P. Lin, Carman A. Puliafito, and James G. Fujimoto, "Optical Coherence Tomography for Ophthalmic Imaging," IEEE ENGINEERING IN MEDICINE AND BIOLOGY, January/February 1995.
11. Daqing Piao, Nan Guang Chen, Quing Zhu, Niloy K. Dutta, Linda L. Otics, "Imaging of Fluid Flow Velocity using Doppler Optical Coherence Tomography: Preliminary Results," Proceedings of the IEEE 27th Annual Northeast bioengineering Conference.
12. Mathieu G. Ducros, Johannes F. de Boer, Huai-En Huang, Lawrence C. Chao, Zhongping Chen, J. Stuart Nelson, Thomas E. Milner, and H. Grady Rylander, III, "Polarzation Sensitive Optical Cohrence Tomography of the Rabbit Eye," IEEE

Journal of Selected Topics in Quantum Electronics, Vol. 5, No. 4, pp. 1159 July/August 1999.
13. Ignacio R. Matias, Manual Lopez-Amo, Fracisco Montero, Carlos Fernandez
14. Valdivielso, Francisco J. Arregui, and Candido Bariain, "Low-Cost Optical Amplitude Modulator Based on a Tapered Single-Mode Optical Fiber," Applied Optics, Vol. 40, No. 2, pp. 228-234, January 10 2001.
15. S.A. Boppart, B.E. Bouma, C. Pitris, G.J. Tearney, and J.G. Fujimoto, "Forward Imaging Instruments for Optical Coherence Tomography," Optics Letters, Vol. 22, No. 21, pp. 1618-1620, November 1 1997.
16. Nelson R. W., Krone JR, Jansson O., "Surfance Plasmon Resonance Biomolecular Interaction Analysis Mas Spectrometry," Anal. Chem. Vol. 69, No. 21, pp. 4369-4374, Nov. 1 1997.
17. Miroslav Sedlar, Vlastimil Matejec, Ivan Paulicka, "Optical Fibre Magnetic Field Sensors Using Ceramic Magnetostrictive Jackets," Sensors and Actuators, Vol. 84 No. 3, pp. 297-302, 2000.
19 Franz Keplinger Samuel Kyasnica, Artur Jachimowicz, Franz Kohl, Johannes Steuer, Hans Hauser, "Loretz Force Based Magnetic Field Sensor with Optical Readout," Sensors and Actuators A. Vol. 110, No. 1-3, pp. 112-118, 2004.
20 C.P.O. Treutler, "Magnetic Sensors for Automotive Applications," Sensors and Actuators A Vol. 91, No. 1-2, pp. 2-6, 2001.
21 John G. Bai, Guo-Quan Lu, Tao Lin, "Magneto-Optical Current Sensing for Applications in Integrated Power Electronics Modules," Sensor and Actuators A Vol. 109, No. 1-2, pp. 9-16, 2003.
22 H.H. Yang, N.V. Myung, J.Yee, D.-Y. Park, B.-Y.Yoo, M. Schwartz, K. Nobe, J.W. Judy, "Ferromagnetic Micromechanical Magnetometer," Sensors and Actuators A Vol. 97-98, pp. 88-97, 2002.
23 M. Sendoh, K. Ishiyama, and K.-I Arai, "Fabrication of Magnetic Actuator for Use in a Capsule Endoscope," IEEE Transactions on magnetics, Vol. 39, No. 5, pp. 3232-3234 September 2003.
24 Shi-Sheng Lee, Ed Motamedi, and Mong C. Wu, "Surface-Micromachined Free-Space Fiber Optic Switches With Integrated Microactuators for Optical Fiber Communication Systems," TRANSDUCERS' 97 1997 International Conference on Solid-State Sensors and Actuators, Chicago, June, pp. 16-19, 1997.
25 Kevin R. Cochran, Lawrence Fan, Don L. DeVoe, "High-Power Optical Microswitch Based on Direct Fiber Actuation," Sensor and Actutors A, Vol.119, No. 2, pp. 512-519, 2005.

26 Mark Herding, Franz Richardt, Peter Woias, "A Novel Approach to Low-Cost Optical Fiber Switches," Optical MEMS, IEEE/LEOS International Conference,2003.
27 Sinji Nagaoka, "Compact Latching-Type Single-Mode-Fiber Switches Fabricated by a Fiber-Mcromachining technique and Their Practical Application," IEEE Journal of Selected Topics in Quantum Electronics, Vol. 5, No. 1, 1999.
28 Naresh Dhaubanjar, "The Design and Analysis of Optical Scanners for Optical Coherence Tomography," UTA Master's report, August, 2006.
29 P.N. Singh. P.K. Jhas, (1980) Elementary Mechanics of Solids, John and Wiley & Son, Inc.
30 R.E. Rosensweig, (1985) Ferrohydrodynamics, Cambridge University Press.
31 J.P. Den Hartog, (1985) Mechanical Vibrations Dover Publications, Inc.
32 Jack W. Judy and Nosang Myung, "Magnetic Materials for MEMS," Electrical Engineering, University of California, Los Angeles, CA, USA. http://www.ee.ucla.edu/~jjudy/publications/conference/mrs_2001_judy_myung.pdf.
33 Fennimore N. Bradley, MATERIALS FOR MAGNETIC FUNCTIONS, Hayden Book Company, Inc, New York. P.38.
34 B.D. Cullity, INTRODUCTION TO MAGNETIC MATERIALS, Addison-Wesley Publishing Company. P. 207-234, 243, 252.
35 David Jiles, Introduction to MAGNETISM and MAGNETIC MATERIALS, 1st ed. Chapman and Hall. P. 38.
36 Carl Chang, "A Magnetically Actuated Scanning Microplatform for Intravascular Ultrasound Imaging," M.S. Report, Department of Electrical Engineering and Computer Science, University of California, Berkeley, 1998.
37 William D. Cllister, JR., Materials Science and Engineering AN INTRODUCTION 4TH edition, John Wiley & Sons, Inc. pp.676-665-666.
38 Marc J. Madau, "Fundamentals of Micro-Fabrication The Science of Miaturization," 2nd edition, CRC Press pp. 350.
39 Mitsunori Saito, Kaoru Nakajima, and Mitsunobu Shishido, "Polymer Coating on Infrared Silever Halide Fiber for Photo Dardening Protection," Journal of Lightwave Technology, Vol. 20, No. 3, March 2002.
40 Gillermo J. Tearney, Mark E. Brezinski, Brett E. Bouma, Stephen A. Boppart, Costas Pitris, James F. Southern, James G. Fujimoto, "In Vivo Endoscopic Optic Biopsy with Optical Coherence Tomography," Science, Vol. 276, June 1997.
41 Mark E. Brezinski, and James G. Fujimoto, "Optical Coherence Tomography: High-Resolution Imaging in Nontransparent Tissue,"IEEE Journal of Selected Topics in Quantum Electronics, Vol. 5, No. 4, pp. 1185-1192, July/August 1999.

42 M. Samir Jafri, Cha-Min Tang, "Optical Coherence Tomography in the Diagnosis and Treatment of Neurological Disorders," Journal Biomedical Optics, Vol. 10, No. 5, September/October 2005.
43 Woongyu Jung, Bunsho Kao, Kristen M. Kelly, Lih-Huei L. Kiaw, J. Stuart Nelson, and Zhongping Chen, "Optical Coherence Tomography for In Vitro Monitoring of Wound Healing After Laser Irradiation," IEEE Journal of Selected Topics in Quantum Electronics, Vol. 9, No. 2, pp. 222-226, March/April 2003.
44 Woonggyu Jung, Jun Zhang, Jungrae Chung, Petra Wilder-Smith, Matt Brenner, J. Stuart Nelson, and Zhongping Chen, "Advances in Oral Cancer Detection Using Optical Coherence Tomography," IEEE Jounal of Selected Topics in Quatum Electronics, Vol. 11, No. 4, pp.811-817 July/August 2005.
45 Nirlep A. Patel, Jason Zoeller, Debra L. Stamper, James G. Fujimoto, and Mark E. Brezinski, "Monitoring Osteoarthritis in the Rat Model Using Optical Coherence Tomography," IEEE Transaction on Medical Imaging, Vol. 24, No. 2, pp. 155-159, February 2005.
46 N.D. Gladkov, G.A. Petrova, N.K. Nikonov, G.V. Gelikonov, R.V. Kuranov, A.M. SerGeev, and F.I. Feldchtein, "In Vivo Optical Coherence Tomography Imaging of Human Skin: Norm and Pathology," Skin Research and Technology, Vol. 6 pp. 6-16, 2000.
47 Yuishi Teramura, Masayuki Suekuni and Fumihiko Kannari, "Two-Dimension Optical Coherence Tomography Using Spectral Domain Interferometry," Journal of optics A: Pure and Applied Optics, Vol. 2, pp. 21-26, 2000.
48 Victor X.D. Yang, Maggie L. Gordon, Bing Qi, Julius Pekar, Stuart Lo, Emily Seng-Tue, Alvin Mok, Brian C. Wilson, and I. Alex Vitkin, "high Speed, Wide Velocity Dynamic Range Doppler Optical Coherence Tomography: System Design, Signal Processing and Preformance," Optics Express, Vol. 11, No. 7, April 2003.
49 Xingde Li, Tony H. Ko, and James G. Fujimoto, "Intraluminal Fiber-optic Doppler Imaging Catheter for Structural and Functional Optical Coherence Tomography," Optics Letters, Vol. 26, No. 23, Demcember 1, 2001.
50 Johannes F. De Boer, Shyam M. Srinivas, B. Hyle Park, Tuan H. Pham, Zhongping Chen, Thomas E. Milner and J. Stuart Nelson, "Polarization Effects in Optical Coherence Tomography of Various Biological Tissues," IEEE Journal of Selected Topics in Quantum Electronics, Vol. 5, No. 4, July/August 1999.
51 Shuguang Guo, Jun Zhang, Lei Wang, J. Stuart Nelson, and Zhongping Chen, "Depth-Resolved Bireference and Diferential Optical Axis Orientation Measurements with Fiber-based Polarization-sensitive Optical Coherence Tomography," Optics Letters, Vol. 29, No.17, Septmeber 1, 2004.

52 Mark. C. Booth, Giovanni Di Giuseppe, Bahaa E.A. Saleh, Alexander V. Sergienko, and Malvin C. Teich, "Polarization-Sensitive Quantum-Optical Coherence Tomography," Physical Review A, Vol. 69 043815, 2004.
53 A.F. Fercher, W. Drexler, C.K. Hitzenberger and T. Laser, "Optical Coherence Tomography-Principles and Applications," REPORTS on PROGRESS IN PHYSICS, Vol. 66, pp. 239-303, 2003.
54 J.M. Zara, S. Yazdanfar, K.D. Rao, J.A. Izatt, and S.W. Smith, "Eletrostatic Micromachine Scanning Mirror for Optical Coherence Tomography," Optics Letters, Vol. 28, No. 8, April 15, 2003.
55 Peter H. Tran, David S. Mukai, Matthew Brenner, and Zhongping Chen, "In Vivo Endoscopic Optical Coherence Tomography by Use of a Rotational Microelectromechanical System Probe," Optics letters, Vol. 29, No. 11, June1, 2004.
56 Yuli Wang, Mark Bachman, and Guann-Pyng Li, Shuguang Guo, Brian J. F. Wong, Zhongping Chen, "Low=Voltage Polymer-based Scanning Cantilever for in vivo Optical Coherence Tomography," Optics Letters, Vol. 30, No. 1, January 1, 2005.
57 Tuqiang Xie, Huikai Xie, Gary K. Fedder, and Yingtian Pan, "Endoscopic Optical Coherence Tomography with a Modified Microelctromechanical Systems Mirror for Detection of Bladder Cancers," Applied Optics, Vol. 42, No. 31, November 1, 2003.

BIOGRAPHICAL INFORMATION

Hans Po-sheng Hu received his Bachelor of Science and Master of Science at the University of California, Irvine in 2001 and 2003 respectively. He then obtained his Ph.D. from the University of Texas, Arlington in 2007. All Degrees are in Electrical Engineering. Hans Po-sheng Hu is interested in a broad spectrum of research fields: optics, magnetism, electromagnetism, biomedical imaging, and microscopy.